Corrosion mechanisms of ferritic-martensitic P91 steel and Inconel 600 nickel-based alloy in molten chlorides. Part I: NaCl–KCl binary system

B. Grégoire, C. Oskay, T.M. Meißner, M.C. Galetz

https://doi.org/10.1016/j.solmat.2020.110659

Corrosion mechanisms of ferritic-martensitic P91 steel and Inconel 600 nickel-based alloy in molten chlorides. Part I: NaCl-KCl binary system

B. Grégoire*, C. Oskay, T.M. Meißner, M.C. Galetz*

DECHEMA-Forschungsinstitut, Theodor-Heuss-Allee 25, 60486 Frankfurt am Main, Germany

* Corresponding authors: benjamin.gregoire85@laposte.net (B. Grégoire), mathias.galetz@dechema.de (M.C. Galetz)

ABSTRACT

With suitable thermophysical properties and commercial viability, molten chlorides are promising candidates to replace nitrate salts as heat transfer fluids (HTF) and thermal energy storage (TES) materials for next-generation concentrated solar power (CSP) plants. Nevertheless, structural materials including steels and nickel-based alloys experience severe corrosion in molten chlorides. The explicit understanding of the corrosion mechanisms is therefore decisive in order to propose viable technical solutions to increase the durability of these materials. In this work, the corrosion behavior of ferritic-martensitic P91 steel and Inconel 600 nickel-based alloy is investigated in molten NaCl-KCl at 700°C under Ar. The salt mixtures after exposure as well as the corroded samples were simultaneously characterized. The systematic metallographic study after the water-free preparation indicates that electrochemical processes play a major role in the overall corrosion mechanisms. In both P91 steel and Inconel 600, the formation of micro-galvanic pairs between Cr-rich phases (anodic sites) and the alloy matrix (cathode) leads to the selective dissolution of Cr from the alloys resulting in the formation of subsurface voids. The influence of O_2 and of various alloying elements on the corrosion kinetics is discussed. Based on the experimental observations, several corrosion mechanisms combining electrochemical reactions, solid-state diffusion and chloridation-oxidation processes have to be taken into account.

Keywords: Concentrated solar power; Molten salts; Chlorides; Corrosion; Galvanic pairs; Thermodynamics

1. Introduction

The increasing demand for renewable energy sources for electricity generation and energy conversion is strongly motivated by environmental and economic concerns [1,2]. Among the possible alternatives to current fossil fuels and non-renewable technologies, solar energy and especially concentrated solar power (CSP) systems are gaining momentum in supplying clean electricity efficiently [1-3]. The CSP technology can also combine electricity generation with seawater desalination and could play a major role in the regions of the world where water scarcity is an important concern for the populations [4-6]. CSP systems use programmable optical devices (mirrors or lenses) to concentrate the solar radiation onto a receiver, which converts light energy into thermal energy through heat transfer fluids (HTF) [3]. The stored thermal energy is then used to produce steam with a heat exchanger, that goes into a conventional steam turbine attached to a generator to produce electricity.

Heat transfer fluids and thermal energy storage (TES) materials must fulfil specific requirements including high thermal conductivity, high heat capacity, low viscosity, low melting point and high boiling point in addition to

commercial viability and limited environmental impact [7-10]. Over the last years, molten nitrate salts have been extensively employed as HTF and for TES owing to their low melting point, high thermal stability up to about 565°C and relatively low costs [3,8,10]. Nevertheless, since the energy conversion efficiency of CSP systems is directly linked to the operating temperature of the molten salt, the next generation of CSP plants is targeted to operate at temperatures over 700°C [9,11,12]. This restricts the use of nitrate salts at such high temperatures, due to their decreasing thermal stability, and substantiates the urgent need in finding alternative HTF and TES materials for higher energy conversion efficiencies [13-16]. To this end, molten chlorides are considered as a promising alternative with high thermal stability, adequate thermophysical properties and lower costs compared to molten nitrates [11-17]. Notwithstanding, the relatively high freezing points of common binary chloride eutectics (e.g. 657°C for NaCl-KCl, 459°C for $MgCl_2$-NaCl or 504°C for $CaCl_2$-NaCl [13]) limit their utilization in industrial CSP applications. Therefore, in common practice, adding a third chloride compound decreases the freezing point without having a significant effect on the decomposition temperature [11,14,15,18]. Consequently, the most promising candidates include the NaCl-KCl-$ZnCl_2$, NaCl-$CaCl_2$-$MgCl_2$ and NaCl-KCl-$MgCl_2$ ternary systems [11,14,18].

Despite the potential of molten chlorides as alternative HTF and TES materials, structural materials experience severe corrosion in chloride mixtures [7,12,16,17,19-21]. This considerably limits the lifetime of structural materials (i.e. iron and nickel-based materials) and thus constitutes one of the greatest challenges in using molten chlorides for next-generation CSP plants. It has long been acknowledged that the level of impurities in chloride melts (e.g. O_2, moisture, metallic and oxide impurities) strongly affects the corrosion rates of metallic alloys [22-24]. For example, Vignarooban et al. have shown that the supply of O_2 molecules has a significant influence on the corrosion kinetics of nickel-based alloys and stainless steels exposed to molten NaCl-KCl-$ZnCl_2$ in sealed containers and in open air containers [7,19]. The authors indicated that such alloys can be used for industrial applications only in anaerobic conditions [7]. However, no precise information on the corrosion mechanisms has been reported in their studies. The undesirable introduction of water and of O_2 in the salt mixtures can be limited to some extent by salt purification methods and the use of an inert atmosphere such as Ar as ullage gas [23,24]. It is usually accepted that water contamination in molten chlorides as moisture releases hydrogen chloride (HCl) by reaction with chloride anions following, respectively, reaction (1) or the hydrolysis reaction (2):

$$H_2O(g) + 2Cl^- \rightleftarrows O^{2-} + 2HCl(g) \quad (1)$$

$$H_2O(g) + Cl^- \rightleftarrows OH^- + HCl(g) \quad (2)$$

The systematic formation of hydrogen chloride gas forces the Deacon reaction (3) to proceed to the right in presence of O_2, i.e. generation of chlorine (Cl_2):

$$4HCl(g) + O_2(g) \rightleftarrows 2Cl_2(g) + 2H_2O(g) \quad (3)$$

Reaction (3) implies an increase in the Cl_2 partial pressure within the salt mixture. Therefore, in many publications [17,20,25], the corrosion attack of metallic materials in molten chlorides was solely attributed to the reactivity of Cl_2 molecules following the generalized reaction [26,27]:

$$M(s) + x/2\ Cl_2(g) \rightleftarrows MCl_x(l,g) \quad (4)$$

where M represents one of the metal alloying elements and MCl_x its corresponding chloride compound.

Depending on the alloying elements and their concentration, several soluble or volatile chloride compounds (e.g. $CrCl_2$, $CrCl_3$, $FeCl_2$ or $NiCl_2$ [26-28]) are expected to form at the metal/salt interface. Finally, the volatile

chloride compounds diffuse towards the salt/gas interface and may be transformed into oxides in regions with sufficiently high O_2 partial pressure releasing gaseous chlorine as described for waste incineration environments [26-29]. This autocatalytic process consisting in the formation of chloride compounds at the metal surface, their volatilization and subsequent oxidation at the outer surface is known as the "active oxidation process" or "chloridation-oxidation" [26-28]. The stability of chloride and oxide species can be predicted by thermodynamics based on their Gibbs free energies of formation [20,27].

Even though chloridation-oxidation mechanisms could play a role in the corrosion processes in molten chlorides, electrochemical processes must also be considered in such systems (i.e. electrolyte in contact with a metallic material) [22]. The electrochemical nature of the corrosion processes for various stainless steels and nickel-based alloys immersed in molten NaCl-KCl was highlighted by Abramov and co-workers [30-32]. These authors indicated that the major corrosion products consist of Fe, Cr and Mn species whereas Ni and Mo are more stable. These systematic observations suggest the preferential anodic dissolution of Fe, Cr and Mn following the generalized reaction (5) and the presence of cathodic sites supporting the reduction of oxidants following reaction (6):

$$M(s) \rightarrow M^{n+} + ne^- \quad (5)$$

$$Ox + ne^- \rightarrow Red \quad (6)$$

where M corresponds to the least noble elements in the electromotive force series (i.e. Fe, Cr or Mn), n is the number of exchanged electrons during the oxidation or the reduction reactions and where *Ox* and *Red* represent the oxidant and its corresponding reductant, respectively. The overall electrochemical corrosion reaction is therefore [24]:

$$M(s) + Ox \rightleftarrows M^{n+} + Red \quad (7)$$

The distribution of anodic and cathodic sites on the alloy surfaces indicate the formation of galvanic pairs upon exposure to molten NaCl-KCl acting as an electrolyte [30-32]. Abramov and co-workers also suggested that phase transformation and carbide precipitation can play an important role in the formation of micro-galvanic pairs in alloys since Cr-rich carbides were usually preferentially attacked by molten chlorides [31-33]. It should be noted here that such galvanic coupling effects are in good agreement with the electromotive force series of metals in molten chlorides with $Mn^{2+}/Mn < Cr^{2+}/Cr < Fe^{2+}/Fe < Cr^{3+}/Cr < Ni^{2+}/Ni$ [34-36]. Similarly, the occurrence of galvanic corrosion in molten fluorides was emphasized by Wang et al. when immersing Ni/Fe, Fe/Cr and Ni/Cr couples in molten LiF-NaF-KF at 700°C [37]. The latter authors observed that Cr is the anode in both Fe/Cr and Ni/Cr couples whereas Fe is the anode for Ni/Fe couple with the largest potential difference between Ni/Cr couple leading to significant galvanic corrosion of Cr [37]. These electrochemical considerations fairly explain the preferential dissolution of Cr, as the most active alloying element, when iron and nickel-based alloys are exposed to molten fluorides [38,39].

Since O_2 is a strong oxidant, increasing the O_2 partial pressure in the ullage gas forces reaction (6) to proceed to the right thereby increasing the cathodic current and, simultaneously, the anodic dissolution of the least noble elements. The reduction of oxygen is generally assumed to follow reaction (8) where the produced O^{2-} anions can react with dissolved metal cations to form oxides, i.e. reaction (9):

$$O_2(g) + 4e^- \rightarrow 2O^{2-} \quad (8)$$

$$xM^{n+} + yO^{2-} \rightleftarrows M_xO_y(s) \quad (9)$$

The introduction of highly hygroscopic salts such as $MgCl_2$ is usually associated with higher corrosion rates because of significant water impurity levels in the salt mixtures leading to hydrolysis reactions [12,16,17,20-22,40], see reaction (2). However, iron and nickel-based alloys also showed high corrosion rates in LiCl-KCl and NaCl-KCl melts [24,25,32]) despite the absence of such hygroscopic components and even with advanced salt purification techniques. Based on the literature review of molten chlorides exposures for CSP applications, it therefore appears that the corrosion mechanisms are still not fully understood and are sometimes contradictory. To the best of the authors' knowledge, no experimental study focused on the simultaneous comprehension of both electrochemical and chloridation-oxidation processes. This study therefore proposes to investigate the corrosion mechanisms of ferritic-martensitic P91 steel and Inconel 600 nickel-based alloy in an inert atmosphere (Ar) with partial embedding in molten NaCl-KCl and in molten NaCl-KCl-$MgCl_2$ at 700°C (targeted operating temperature for the next generation of CSP plants [12,16,17]). The systematic comparison of the corrosion behavior of these two alloys in molten NaCl-KCl and in molten NaCl-KCl-$MgCl_2$ was expected to further emphasize the influence of electrochemical processes and of impurities on the corrosion mechanisms. For the sake of clarity, this study was divided in two distinct papers with the present one focusing on the NaCl-KCl system. Understanding the fundamental corrosion mechanisms occurring upon exposure of metallic materials in molten chlorides will help to propose adequate solutions to mitigate the corrosivity of molten chlorides and further develop material selection and surface treatments.

2. Experimental procedures

2.1. Materials

As-received metallic plates of ferritic-martensitic P91 steel (Vallourec) and Inconel 600 (VDM Metals) materials were machined into rectangular samples with, respectively, 25 mm x 6 mm x 3 mm and 25 mm x 5 mm x 3 mm dimensions. The nominal and tested chemical compositions of the two commercial alloys are given in Table 1. Optical emission spectrometry (OES) measurements were performed with a SPECTROMAXx analyzer from SPECTRO Analytical Instruments GmbH (Kleve, Germany). Inconel 600 is a reasonable choice for exposure to molten chlorides at 700°C owing to its relatively lower Cr content, which led to its higher corrosion resistance than Inconel 625 in chloride melts [23,41]. Although P91 substrate is usually employed at temperatures up to about 650°C for industrial applications, its low concentration of alloying elements was expected to simplify the understanding of the corrosion mechanisms in molten chlorides. In addition, both alloys are TES containment material candidates for CSP applications [9].

Table 1
Nominal and tested chemical compositions of the two commercial alloys used in this study (wt.%). OES: optical emission spectrometry.

Alloy	Composition	Fe	Cr	Ni	Mo	Mn	V	Ti	Si	C	Other
P91 (1.4903)	Nominal	Bal.	8.0-9.5	≤ 0.40	0.85-1.05	0.30-0.60	0.18-0.25	-	0.20-0.50	0.08-0.12	Nb: 0.06-0.10
	OES	89.0	8.7	0.20	0.84	0.43	0.20	-	0.24	0.08	Nb: 0.08
Inconel 600 (2.4816)	Nominal	6.0-10.0	14.0-17.0	Bal.	-	≤ 1.00	-	≤ 0.30	≤ 0.50	≤ 0.15	Cu: ≤ 0.50
	OES	8.3	17.1	73.2	-	0.25	-	0.21	0.40	0.04	Cu: 0.07

For microstructural observations, one sample of each substrate was hot embedded in a resin containing graphite and ground with progressively finer SiC paper down to P4000. After polishing with a 1 µm diamond suspension and a 0.04 µm colloidal silica suspension (OP-S, Struers), the samples were electrochemically etched with 10% oxalic acid to reveal the as-received microstructures (Fig. 1). The distribution of alloying elements within the base material, especially Cr, is expected to impact their corrosion behavior since the attack in molten chlorides is usually associated with the selective dissolution of Cr [12,16,17,21,32]. As shown in Fig. 1a, P91 possesses a uniform tempered lath martensitic microstructure with distribution of $M_{23}C_6$ (with M: Cr, Mn, Fe, Mo) carbides within lath boundaries, subgrain interiors and at the prior austenite grain boundaries (PAGBs) [42,43]. The grain size of as-received P91 varied from approximately 5 to 25 µm. Inconel 600 presents larger grains ranging from approximately 20 to 200 µm (Fig. 1b). The main phase in Inconel 600 is a γ-solid solution based on nickel. Intergranular carbides associated with Cr enrichments can be observed at the grain boundaries (GBs) indicating the precipitation of Cr_7C_3 particles as observed in Ref. [44].

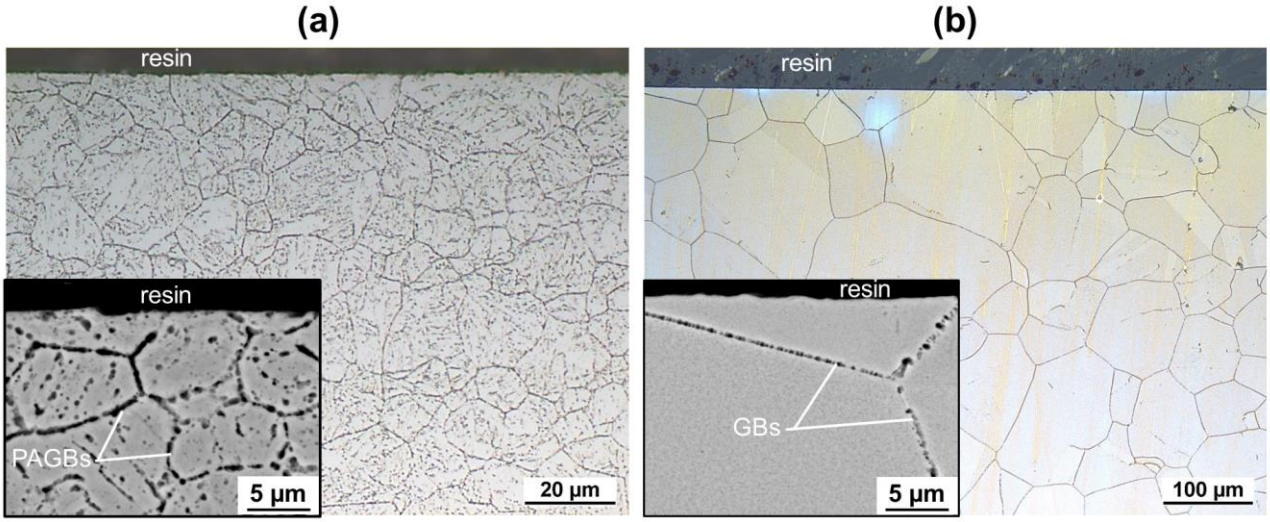

Fig. 1. Light optical microscope cross-section images of as-received (a) ferritic-martensitic P91 steel (x500 magnification) and (b) Inconel 600 (x100 magnification) after electrochemical etching with 10% oxalic acid. Corresponding BSE cross-images at x5000 magnification are also given in the insets. PAGBs: prior austenite grain boundaries, GBs: grain boundaries.

2.2. Corrosion tests in molten salt environment

To facilitate the positioning of the samples in the salt mixtures and avoid galvanic coupling effects [22,39], the metallic samples were drilled on one side and hang vertically with alumina rods (FRIATEC, diameter: 1.5 mm), see Fig. 2a. For this, two slits were carved on cylindrical alumina crucibles (FRIATEC, height: 40 mm, external diameter: 30 mm) with a wet tile saw blade to fix the alumina rods. Before the corrosion experiments, all alumina parts were baked in air at 1000°C for 24 h following ISO 17245 [45]. Each metallic sample was subsequently ground with P1200 SiC paper on all faces, rinsed with distilled water and ultrasonically cleaned in ethanol. Before exposure, all dimensions of the samples were measured with a digital micrometer (mean of 5 different measurements with a maximum deviation of ± 5 µm). The samples were ultrasonically cleaned in ethanol and dried a second time right before embedding in the salt mixture.

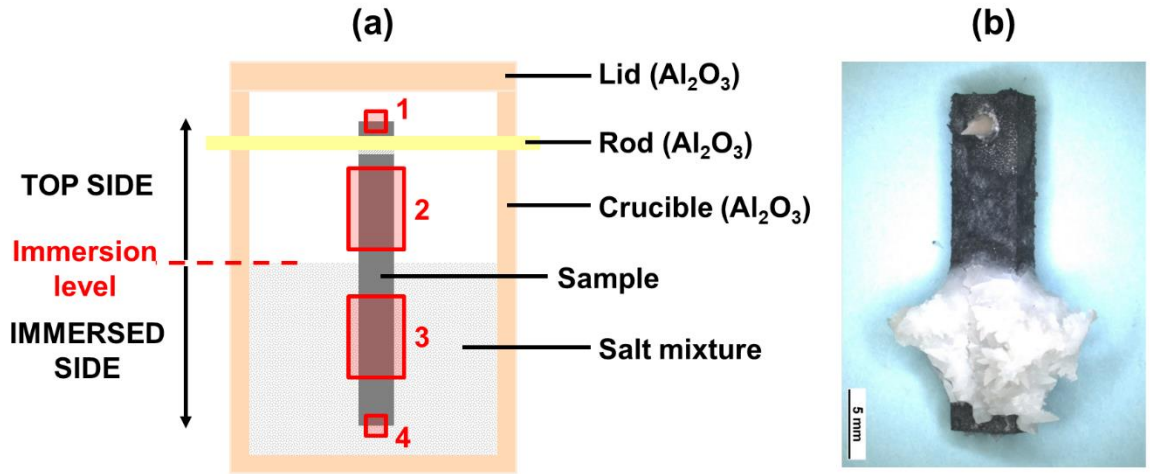

Fig. 2. (a) Schematic representation of the experimental set up for the molten salt exposure and (b) corresponding macrograph of a P91 sample after partial embedding in molten NaCl-KCl for 300 h at 700°C showing the remaining salt mixture attached to the sample. The locations 1 to 4 correspond to the areas of investigation with, respectively, 1: top edge, 2: outer region, 3: immersed region and 4: bottom edge.

NaCl and KCl anhydrous salts (> 99 wt.% purity) were purchased from Alfa Aesar, Germany. The investigated salt mixtures were prepared in hermetic plastic containers by weighing the desired amounts of salts according to the eutectic ratio given in Table 2. The salt mixtures were thoroughly mixed for 2 h in a planetary mixer before use. The metallic samples were then positioned in the alumina crucibles containing approximately 19 g of the salt mixture. The partial embedding of the samples (Fig. 2a) allowed the characterization of different regions on the samples, as presented in Refs. [46,47]. This experimental design was expected to give valuable information on the corrosion kinetics and the corrosion mechanisms of the alloys because of different local thermodynamic conditions (i.e. access of O_2 and/or H_2O molecules and physical/electrical contact with the molten salt). This design was also expected to highlight the influence of electrochemical and/or chloridation-oxidation processes on the corrosion mechanisms involved. Such differences could simulate the alternative filling and emptying of the HTF associated with the day/night cycles in molten salt reservoirs. In fact, the regions that are alternatively immersed in the molten salt (day) and exposed to the gas phase (night) are expected to undergo different corrosion processes, as commonly observed for metallic structures in the sea water tidal zones with wet/dry cycling periods [48,49].

Table 2
Composition of the chloride mixture used in this study.

Salt mixture	Composition		$T_{eutectic}$ (°C)	
	(wt.%)	(at.%)	Theoretical	Experimental
NaCl-KCl	44.5-55.5	50.6-49.4	657 [50]	657 [51]

For each corrosion test, four alumina crucibles were systematically placed in two different alumina boats (two samples for each material) and placed in the hot zone of a horizontal furnace with a quartz tube. Prior to the testing, the temperature profile of the furnace has been monitored with a Type-S thermocouple to determine the width of the isothermal zone, with a tolerance of ±4°C at 700°C according to ISO 17245 [45]. After introduction of the crucibles at room temperature, the furnace was purged with Ar (5 ppm water vapour + 2 ppm O_2) at 12 L/h to remove the atmospheric contaminants. The Ar flow rate was then decreased to 1.8 L/h before the heating procedure and the absolute pressure of the furnace was maintained slightly above the atmospheric pressure. Following Ding et al. [12,16], the furnace was heated at 5°C/min up to 200°C, held at 200°C for 1 h to remove residual water and further heated at 5°C/min up to 700°C. The isothermal corrosion tests were then carried out at 700°C for 20, 100 and 300 h under flowing Ar (1.8 L/h).

2.3. Dimensional metrology and characterization methods

In the literature, the corrosion rates of materials exposed to molten chlorides are very often calculated from weight change measurements [20,21]. However, this method does not seem to be appropriate in the case of molten chloride exposures since scale formation (i.e. weight gain), intergranular attack and/or dissolution of the substrate (i.e. weight loss) occur simultaneously. Metal loss measurements, usually employed for Type-II hot corrosion experiments [52-55] are therefore expected to better describe the corrosion behavior of the alloys. Furthermore, very few studies included the characterization of the salt mixture after exposure since the samples are usually cleaned with acids [12] or with deionized water [16,17,21] to remove the residual salt after exposure. This study therefore proposes to combine the analyses of the corroded materials as well as of the salt for a better comprehension of the corrosion mechanisms (see Fig. 2b). To this end, the samples were cold-embedded under vacuum right after the corrosion experiments to prevent the absorption of water molecules and the dissolution of the salt mixtures. Particular care was taken in the preparation of the cross-sections to ensure that the samples are mounted and polished parallel to the longitudinal section, as described in the norm ISO 26146 [56]. A water-free preparation using petroleum oil as lubricant [57] was then conducted by grinding down to P2400 SiC paper. The subsequent polishing was carried out with a 3 µm and a 1 µm diamond finish solutions after drying of the polishing cloths. The samples were systematically cleaned with dry acetone containing molecular sieve. The water-free metallographic preparation preserved the quenched microstructure of the salt in contact with the alloy samples and enabled the characterization of the corrosion scales and leached corrosion products simultaneously by microstructural investigations. To the best of the authors' knowledge, such microstructures have not been presented in details in the literature and give valuable information on the corrosion mechanisms. Between the characterization steps, the samples were stored in desiccators to prevent moisture absorption and were prepared again when required in order to investigate "fresh" cross-sections.

The corroded samples were first systematically characterized by light optical microscopy (LEICA DMLA). For the metal loss measurements, several images at x50 magnification were taken and 100 individual measurements were performed for each section/area. The experimental data set was then plotted on probability plots, following ISO 26146 [56], with a total of 200 measurements for each testing condition (two individual samples per alloy and per exposure time). These probability plots are particularly interesting to depict if the data is fitting a Gaussian distribution (i.e. straight line whose slope corresponds to the standard deviation of the data set). Any deviation from a straight line indicates a second distribution in the data set and can be interpreted, for example, as pitting, grain boundary attack or passivation. Further information is given in Refs. [52-54] to describe the dimensional metrology method.

Scanning electron microscopy (SEM) and Energy-dispersive X-ray spectroscopy (EDX) analyses were carried out at 20.0 kV with a PHILIPS XL40 microscope equipped with an EDAX detector. Electron probe microanalysis (EPMA; JEOL JXA-8100) was conducted at 15.0 kV to observe the cross-section of the corroded samples and to give high resolution elemental mappings. To perform SEM and EPMA observations in high vacuum, the cross-sectioned samples were sputtered with a thin conductive layer of graphite. Because it would have been necessary to clean the salt residues attached to the samples with water to perform X-ray diffraction (XRD) of the surfaces (see Fig. 2b as an illustration), thereby loosing significant information on the corrosion products, it was instead decided to analyze the residual salt mixtures left in the alumina crucibles to identify detached and/or leached corrosion products. For this purpose, the salt residues were first milled in an agate mortar with a pestle and placed in the diffractometer at ambient temperature. The analyses were performed with a BRUKER D8 Advance diffractometer

with LYNXEYE 1D mode in the Bragg-Brentano configuration using Cu $K_{\alpha 1}$ radiation (0.15406 nm). Complementary Raman analyses were conducted with a RENISHAW inVia micro-spectrometer working with a He-Ne laser (632.8 nm).

3. Results

3.1. Analyses of the residual salt mixtures after exposure

The residual salt mixtures left in the crucibles were systematically analyzed by XRD to identify the crystal structures after the corrosion tests. After exposure of both P91 (Fig. 3a) and Inconel 600 (Fig. 3b) substrates to molten NaCl-KCl, the cubic face centered halite (NaCl) and sylvite (KCl) structures were systematically observed with no hydrated compound. An additional crystal structure, identified as Rinneite ($K_3NaFe^{2+}Cl_6$, i.e. $3KCl.NaCl.FeCl_2$), was observed for the residual salt mixtures of P91 and, to a lower extent, Inconel 600 samples. In addition, the crystal structure of Cr_2O_3 was identified for the residual salt mixtures collected from Inconel 600 samples after 100 and 300 h exposure (Fig. 3b). Nevertheless, a comparison of the relative intensities of the diffraction peaks with the powder diffraction file database suggests that these additional compounds represent a small fraction (1 to 3%) of the volume analyzed by XRD. Therefore, additional SEM observations of the salt mixtures were conducted in cross-section and confirmed the presence of Rinneite (Fig. 4a) and of Cr_2O_3 (Fig. 4b) highlighted with a chemical contrast in BSE mode. The stoichiometry of both compounds was ascertained by EDX spot analyses. Metallic Ni-rich particles, appearing bright in BSE, are also observed in Fig. 4b. These observations

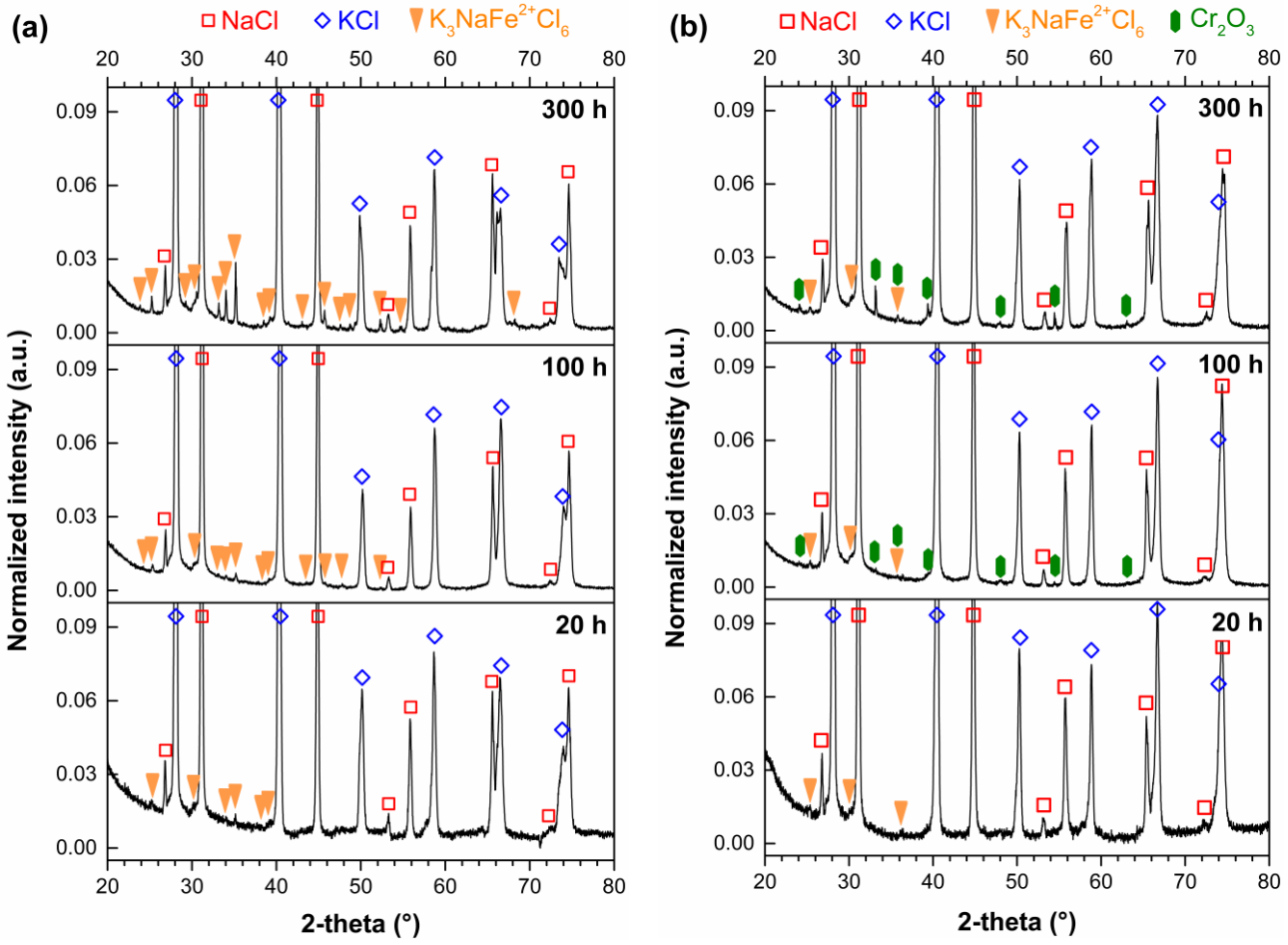

Fig. 3. X-ray diffraction patterns of the salt residues obtained after exposure of (a) P91 and (b) Inconel 600 to molten NaCl-KCl at 700°C in flowing Ar for 20, 100 and 300 h.

suggest that Ni is not or only partially dissolved within the melt whereas Fe is dissolved as Fe^{2+} (i.e. $FeCl_2$) leading to the formation of Rinneite upon cooling. The BSE mode also enabled to distinguish Na(K)Cl (solid solution of KCl in NaCl) and K(Na)Cl (solid solution of NaCl in KCl) crystallites as, respectively, darker and brighter phases in the crystallized microstructure (solid solution transformation at about 505°C [50,51]).

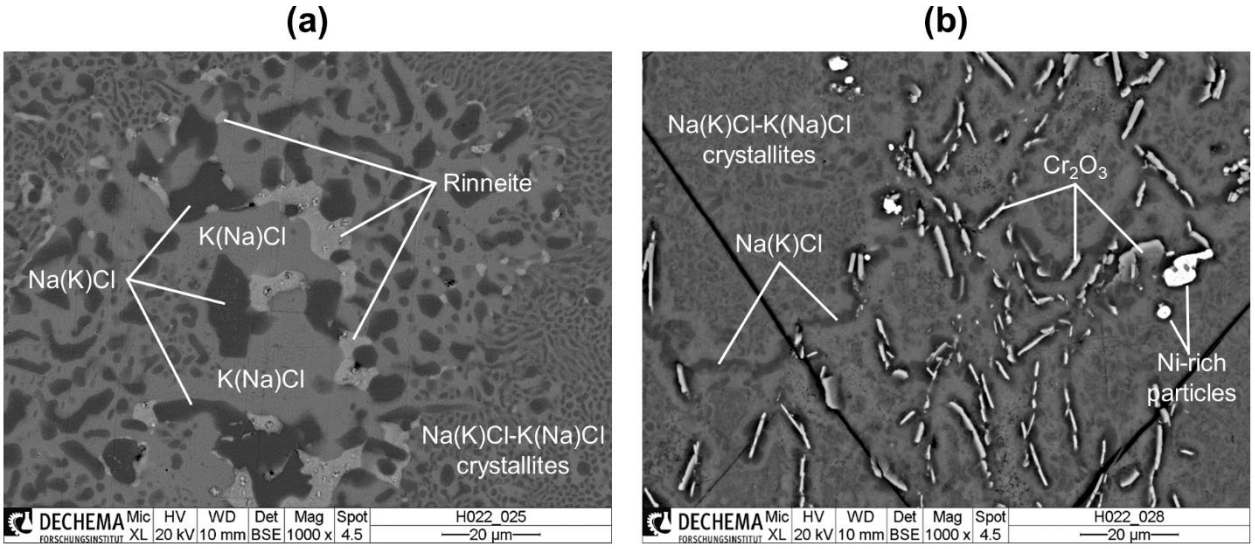

Fig. 4. BSE cross-section images of the residual salt mixtures taken in representative areas after exposure of (a) P91 and (b) Inconel 600 to molten NaCl-KCl at 700°C in flowing Ar for 300 h.

3.2. Metal loss measurements and corrosion rates

Fig. 5 presents the metal loss measurements of P91 and Inconel 600 materials after exposure to molten NaCl-KCl at 700°C and the corresponding light optical micrographs of the investigated regions after 300 h. To highlight the influence of the local thermodynamic conditions, the metal loss measurements were performed on the top side (i.e. initially exposed to the gas only, location 2 in Fig. 2a) and on the immersed side (i.e. initially embedded in the salt, location 3 in Fig. 2a). The distribution of the metal loss values shows that the corrosion behavior of P91 and Inconel 600 is quite different in molten NaCl-KCl. On one hand, the probability plots fit a Gaussian distribution for Inconel 600 (Fig. 5b) appearing as a straight line whose slope corresponds to the standard deviation of the data set [56]. This indicates that Inconel 600 is not prone to pitting but to a progressive corrosion attack with increasing exposure time associated with void formation, as observed after 300 h exposure on Fig. 5d. Inconel 600 is more sensitive to corrosion on the immersed side with a maximum depth of attack of 330 µm after 300 h exposure. On the other hand, the data sets are not fitting a Gaussian distribution for P91 samples exposed to molten NaCl-KCl (Fig. 5a) and the deviation from a straight line indicates the appearance of a second distribution associated with pitting (Fig. 5c). The fraction of pitting areas can be estimated from the probability plots and is found to increase with increasing exposure time. This fraction reaches approximately 10% on the immersed side and 60% on the top side after 300 h exposure of P91 to molten NaCl-KCl at 700°C (Fig. 5a). Unlike Inconel 600, P91 is more sensitive to corrosion above the salt immersion level and a maximum depth of attack of 510 µm was measured in such conditions after 300 h of exposure. The metal loss measurements clearly indicate that both P91 and Inconel 600 alloys do not form protective oxide scales after prolonged exposure to molten NaCl-KCl at 700°C.

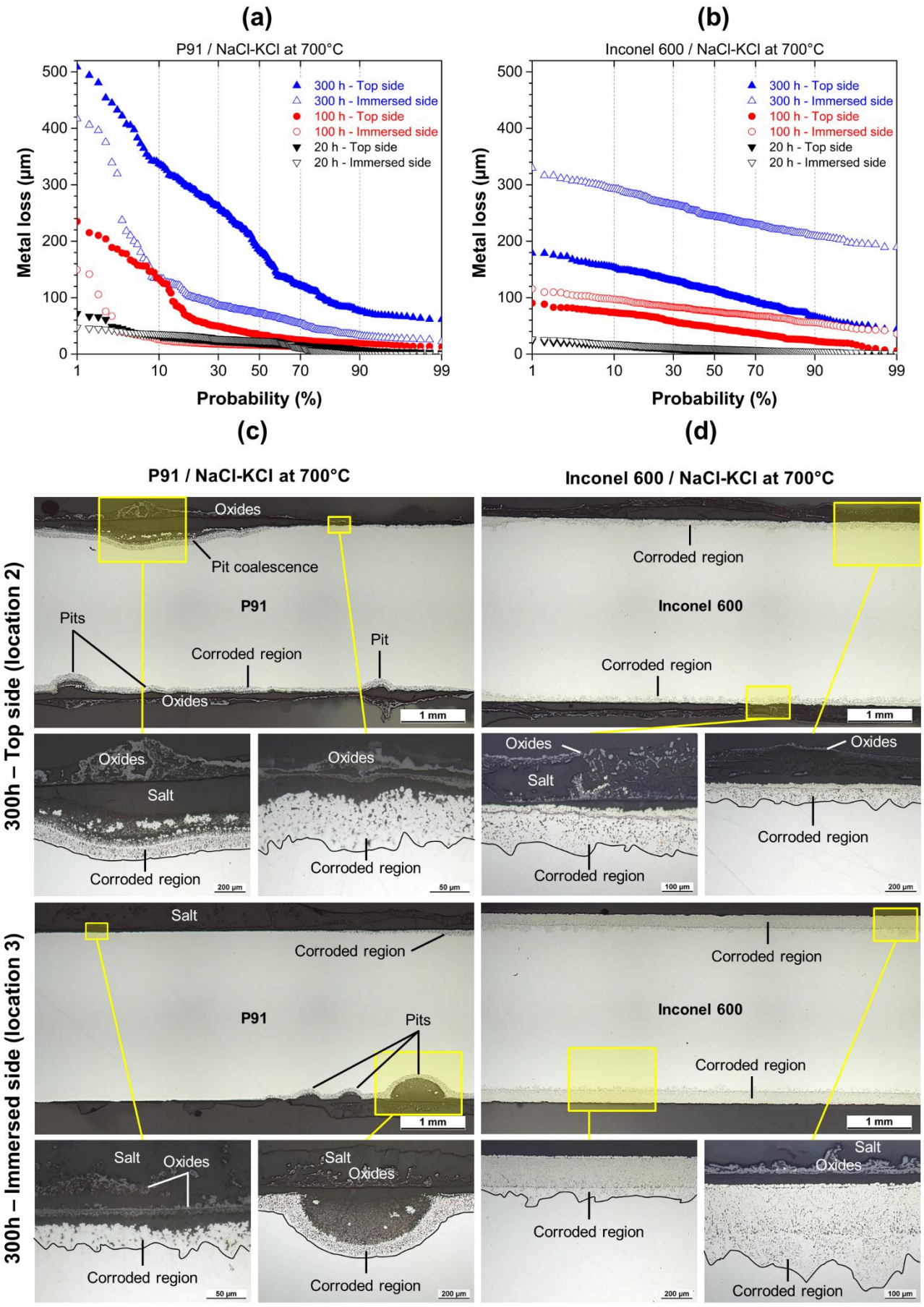

Fig. 5. Probability plots of the metal loss values of (a) P91 and (b) Inconel 600 materials after exposure to molten NaCl-KCl at 700°C in flowing Ar and (c), (d) corresponding cross-section light optical micrographs after 300 h exposure (see Fig. 2a for the selected locations).

The median metal loss and corresponding standard deviation values were determined from the probability plots and are summarized in Fig. 6. Following ISO 26146 [56], the standard deviation values were obtained by linear fitting for each distribution. Since a second distribution related to pitting corrosion was systematically observed for P91 samples (see Fig. 5a), two individual measurements are reported as stack columns in Fig. 6a. The localized character of pitting corrosion explains the relatively high standard deviation values of P91 samples exposed to molten NaCl-KCl after 100 and 300 h exposure.

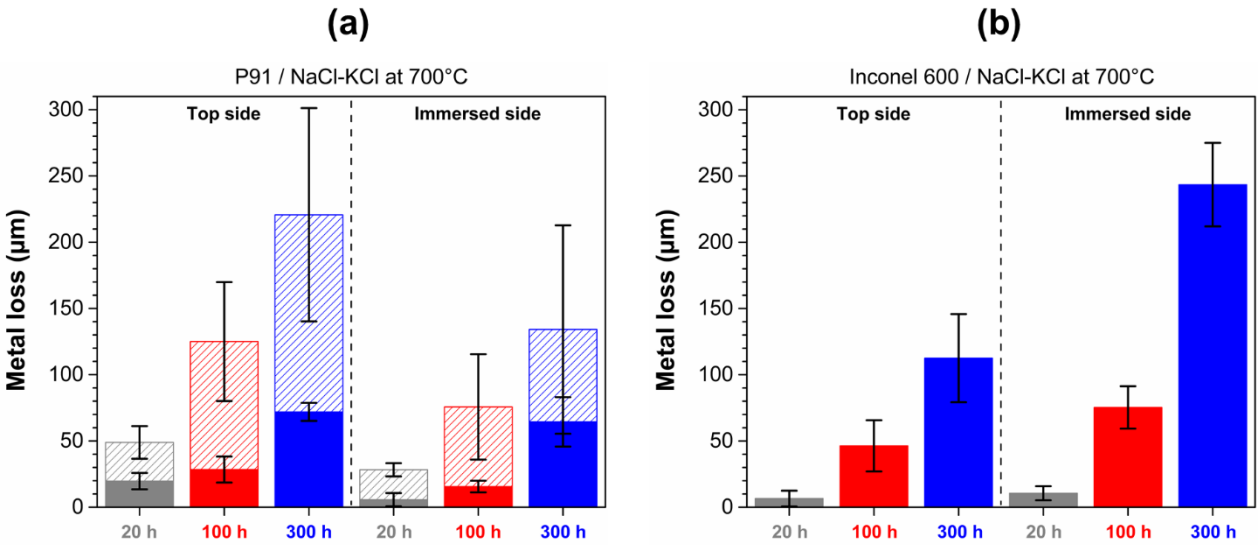

Fig. 6. Summary of median metal loss measurements with standard deviation for (a) P91 and (b) Inconel 600 materials after 20, 100 and 300 h exposure to molten NaCl-KCl at 700°C in flowing Ar. Hatched columns on Fig. 6a correspond to the metal loss values including the pit regions.

The corrosion rates of both alloys on the top side and on the immersed side were calculated from the iso-probability curves of metal loss values as a function of exposure time (Fig. 7) following the work of Sumner et al. [53]. Hot corrosion damages are usually divided into incubation and propagation stages. Therefore, the corrosion model presented in Eq. (10) is based upon the metal loss (ML) rate in the incubation stage (k_{inc}), the ML rate in the propagation stage (k_{prop}) and the duration of the incubation period, noted t_{inc}, when there is a transition between the two stages:

$$ML = k_{inc}.t_{inc}^{m} + k_{prop}.(t-t_{inc})^{n} \quad (10)$$

where m and n are the respective exponential coefficients.

In specific conditions with aggressive deposits such as molten chlorides, the incubation period is close to zero and thus the experimental data can be fitted to curves in the form:

$$ML = k.t^{n} \quad (11)$$

For clarity, only five iso-probability curves were plotted for each testing condition (i.e. 5%, 25%, median, 75% and 95%) in Fig. 7. Taking into consideration the erratic character of corrosion damages, this representation is particularly helpful to discriminate the corrosion behaviour of a material in a given condition. For each testing condition, the experimental data were fitted to power-law curves following Eq. (11) where the n value corresponds to the best fit curve as presented in Ref. [53]. Each iso-probability curve indicates the probability for a metal loss value to be lower or higher than a given value as a function of exposure time. As an example, the probability for a metal loss exceeding 200 µm for Inconel 600 after 300 h exposure in NaCl-KCl melt at 700°C is 95% whereas the

probability is only 5% for a metal loss exceeding 300 µm in similar conditions (see Fig. 7d). The corresponding per annum corrosion rates obtained by extrapolation of the iso-probability curves after one year for 5%, median and 95% are reported on the graphs for each testing condition. The estimated corrosion rates of Inconel 600 in molten NaCl-KCl (Fig. 7d) are significantly higher than the ones of ferritic-martensitic P91 steel (Fig. 7c). Nevertheless, the deviation in the metal loss values is much larger for P91 than Inconel 600, which indicates the susceptibility of P91 to pitting corrosion with localized high corrosion rates (see 5% iso-probability curves in Fig. 7a and Fig. 7c). Even though the formation of pits is clearly the life-limiting parameter for P91, Inconel 600 shows overall more metal loss due to corrosion, especially in the melt (i.e. immersed side). Further information will be given in section 4.1. to explain such differences.

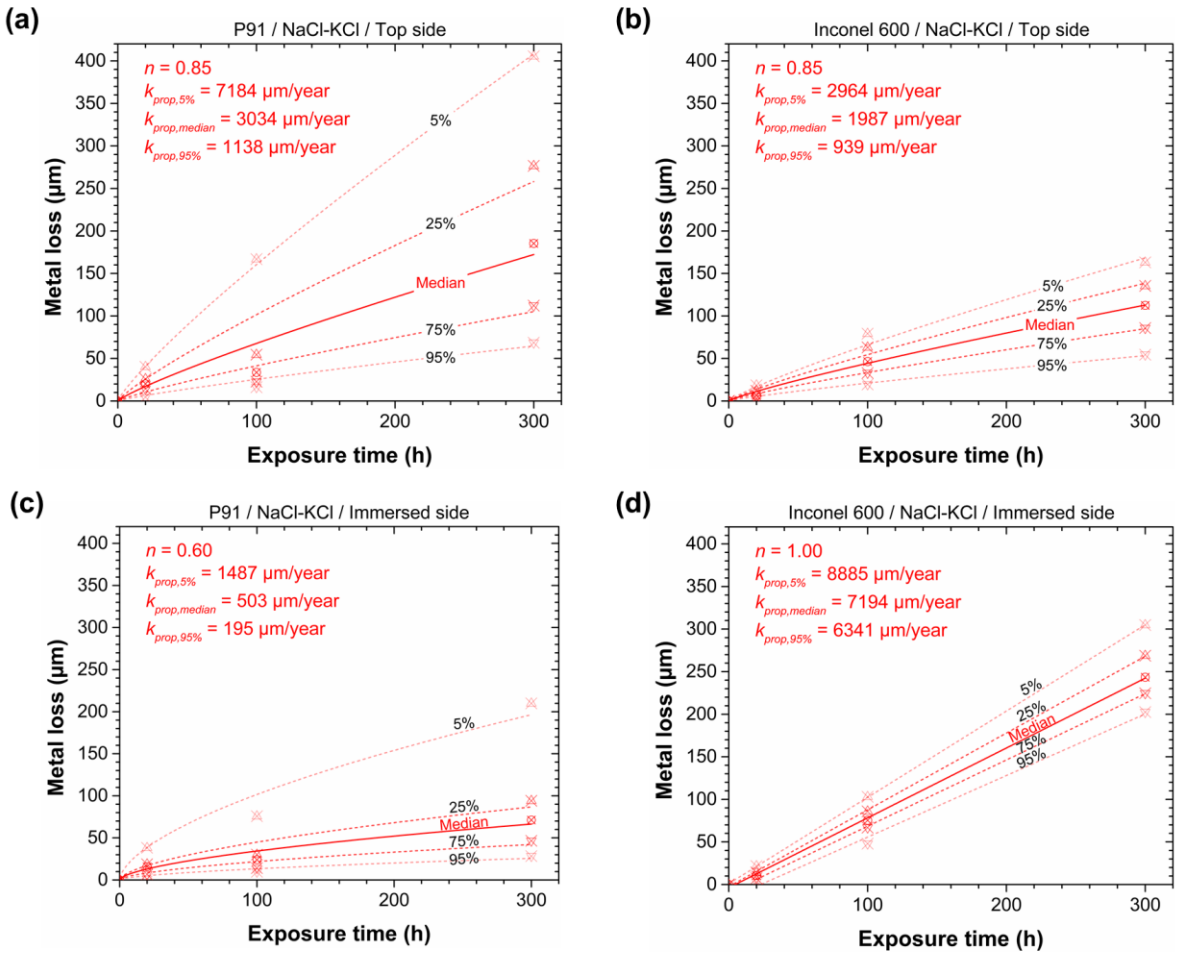

Fig. 7. Iso-probability curves of metal loss values as a function of exposure time for (a), (c) P91 and (b), (d) Inconel 600 alloys exposed to molten NaCl-KCl at 700°C in flowing Ar. (a), (b) top side corresponds to location 2 in Fig. 2a and (c), (d) immersed side corresponds to location 3 in Fig. 2a. Points indicate experimental data and lines the best fit curves. For each testing condition, the *n* values as well as the estimated propagation rates corresponding to 5%, median and 95% iso-probability curves are reported on the graphs.

3.3. Microstructural characterization of the corroded samples

3.3.1. Ferritic-martensitic P91 steel

To further investigate the corrosion behavior of ferritic-martensitic P91 steel, representative images were taken at the different locations highlighted in Fig. 2a after 100 and 300 h exposure at 700°C in flowing Ar (Fig. 8). One can first see that the corrosion attack increases with increasing exposure time for all locations, which indicates that P91 does not form protective oxide scales in such conditions. As deduced from metal loss measurements in Fig. 6a and Fig. 7a, P91 samples are more sensitive to corrosion in the top half (locations 1 and 2 in Fig. 2a) than in the immersed half (locations 3 and 4 in Fig. 2a). Nevertheless, the corrosion attack seems to systematically propagate at the prior austenite grain boundaries (PAGBs) regardless of the sample location (Fig. 8). Depending on the sample location, the progressive dissolution of the grain boundaries results in a porous substrate region with a thickness ranging from approximately 10 µm (Fig. 8e) to 80 µm (Fig. 8d). Local EDX analyses in the metallic substrate indicates that the porous substrate region contains less than 1 at.% of Cr whereas P91 contains about 9 wt.% of Cr (i.e. ≈ 9 at.%). This suggests that the substrate is progressively depleted in Cr over time.

The corrosion scales formed on the surface of P91 are systematically composed of an inner porous $FeCr_2O_4$ layer with V and Mn enrichments. At higher magnification, fine Mo-rich particles can also be observed within the porous $FeCr_2O_4$ layer (Fig. 8b). Depending on the sample location, large $FeCr_2O_4$ crystals formed on top of the porous $FeCr_2O_4$ layer (visible on Fig. 8a, c, d, e and g). The growth kinetics of such large crystals was presumably very high and did not provide a protective behavior to the underlying substrate. The observation of a porous $FeCr_2O_4$ layer on the surfaces suggests that this layer was in contact with the substrate upon exposure. However, its adherence to the substrate was low, which resulted in the incorporation of the salt into the gap between the porous $FeCr_2O_4$ layer and the substrate. The large cracks observed within the salt mixtures (Fig. 8c, d e and f) most likely indicate that mechanical stresses developed upon cooling because of the high coefficient of thermal expansion (CTE) mismatch between the different phases and the volume difference related to the crystallization of the salt. The difference in microstructure of the salt mixtures after cooling between Fig. 8e and Fig. 8f was associated with the larger fraction of Rinneite ($K_3NaFe^{2+}Cl_6$) within the melt after 300 h of exposure. In fact, as observed in Fig. 4a, the presence of $FeCl_2$ within the melt changes the Na(K)Cl-K(Na)Cl crystallite size after cooling to room temperature.

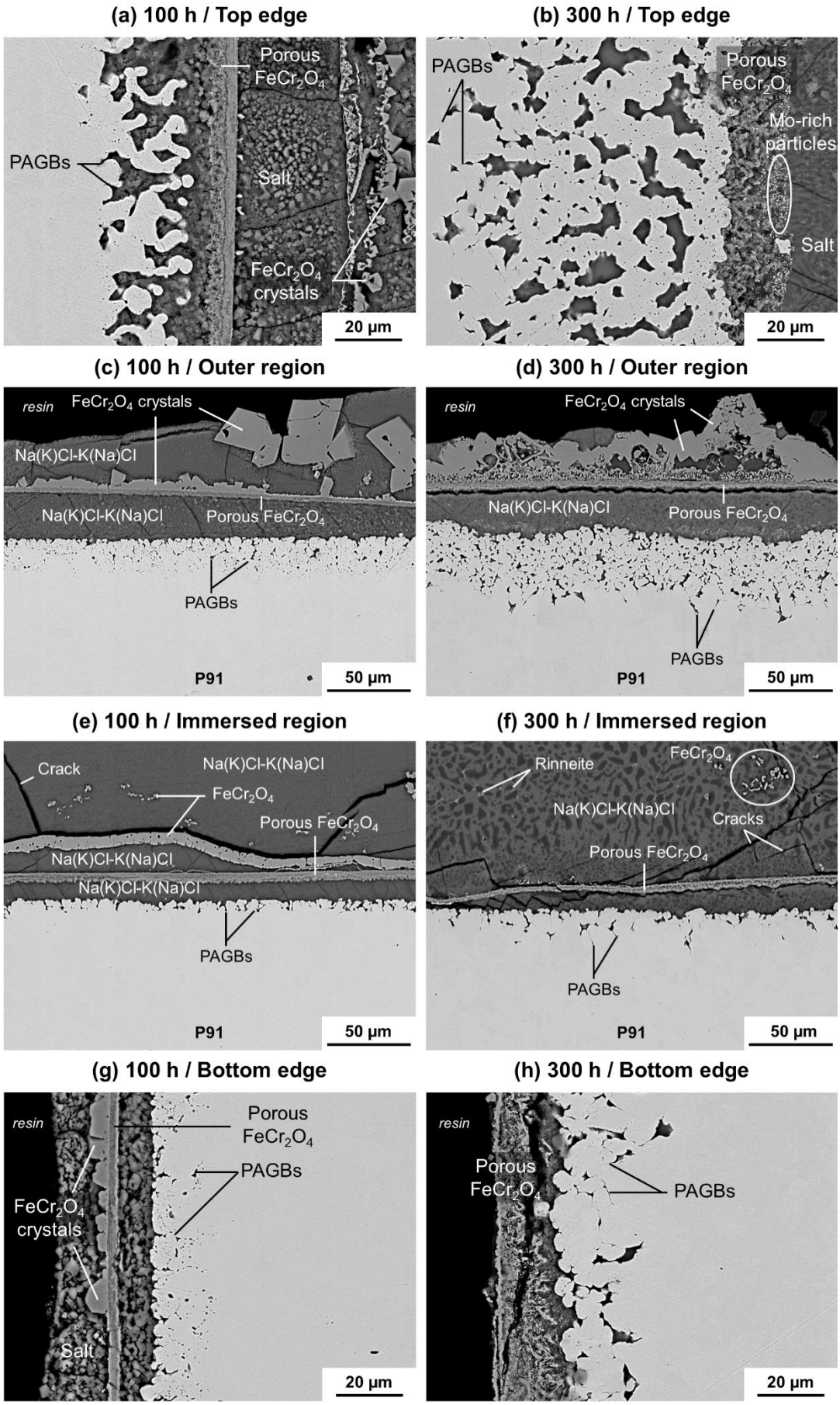

Fig. 8. BSE cross-section images of P91 samples after (a), (c), (e), (g) 100 h and (b), (d), (f), (h) 300 h exposure to molten NaCl-KCl at 700°C in flowing Ar in the different locations given in Fig. 2a.

Whereas most of the material surface suffered from a relatively homogeneous corrosion attack, P91 steel was also prone to pitting corrosion in molten NaCl-KCl (see Fig. 5a and Fig. 5c). To highlight the influence of alloying elements on such behavior, EPMA elemental mappings were performed in a pit region (Fig. 9a) and in a region with more uniform corrosion (Fig. 9b). In both regions, one can see the formation of an inner Fe and Cr-rich oxide layer corresponding to the $FeCr_2O_4$ spinel with large oxide crystals formed above. The Cr and Fe distribution in the oxide crystals emphasizes the formation of both Cr_2O_3 and $FeCr_2O_4$ spinel crystals (see the inset at higher magnification in Fig. 9b). The identification of the oxide compounds was further ascertained by local EDX measurements and Raman spot analyses (see Fig. 10 and Table 3). It should be pointed out that the volume fraction of $FeCr_2O_4$ spinel (i.e. light region in BSE) was considerably larger than the volume fraction of Cr_2O_3 (i.e. dark region in BSE) on most of the P91 samples' surface, as illustrated with the cross-comparison of Fe and Cr maps in Fig. 9b and BSE cross-section images of Fig. 8a-f. Despite the low V content of P91 (≤ 0.25 wt.%), its distribution within the oxide scales is clearly observed in Fig. 9a and Fig. 9b. The EPMA elemental mappings also indicate that the corroded region of the substrate (i.e. porous metallic layer) is depleted in Cr (see Cr map in Fig. 9b), which conversely increased the Ni content in this region. Interestingly, the distribution of Mo is very different in the two regions. Whereas Mo is distributed within the salt in the pit region together with Fe (and to a lesser extent with Ni) in Fig. 9a, the subsurface of P91 is enriched in Mo in Fig. 9b. This major difference could explain the higher corrosion resistance in region b compared to region a. The elemental distribution maps of Cl, Na and K suggest that the molten salt was filling the pores of the corroded regions and that the electrolyte was in contact with the substrate upon exposure.

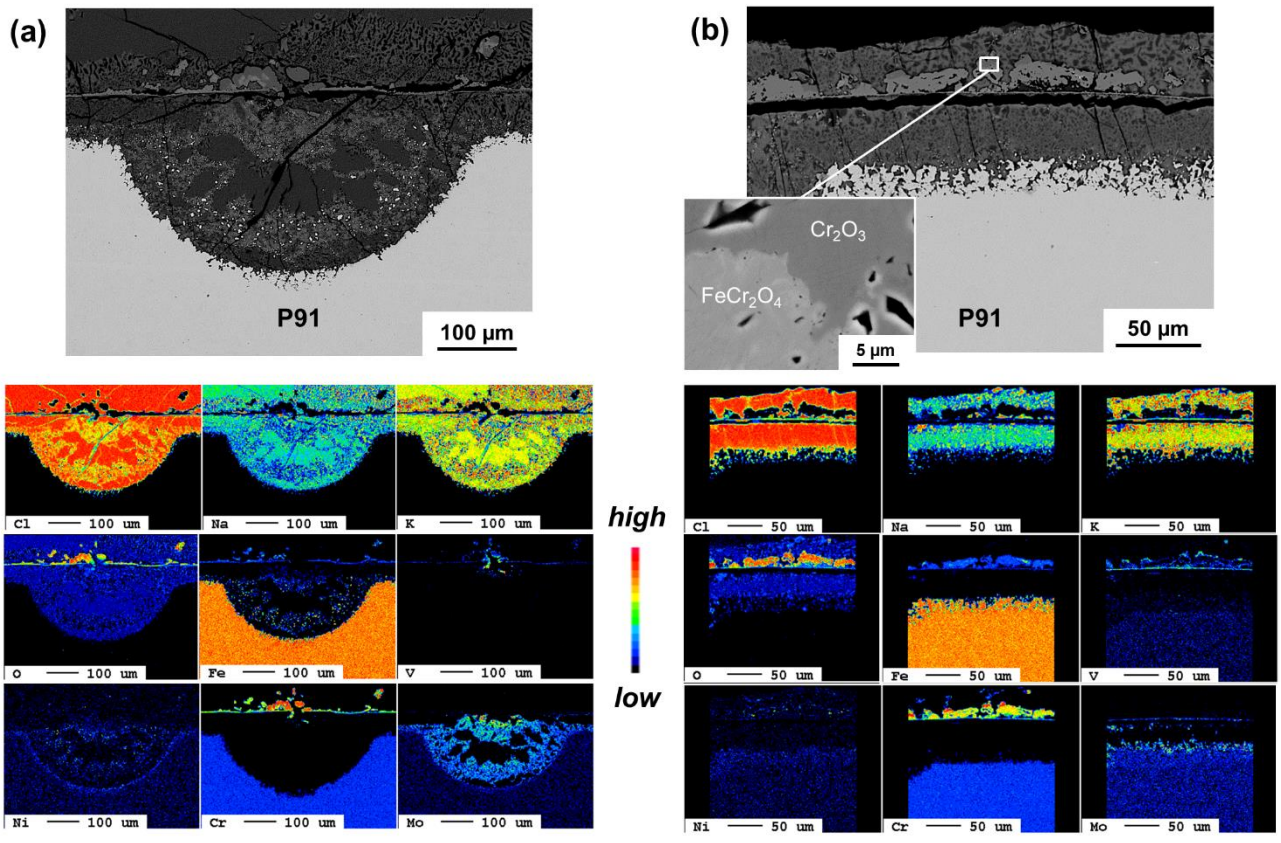

Fig. 9. BSE cross-section images and corresponding EPMA elemental mappings of P91 after 100 h exposure to molten NaCl-KCl at 700°C in flowing Ar in (a) a pit region (location 3) and (b) a region with more uniform corrosion (location 2). The inset highlights the chemical contrast existing in BSE mode between Cr_2O_3 and $FeCr_2O_4$ crystals.

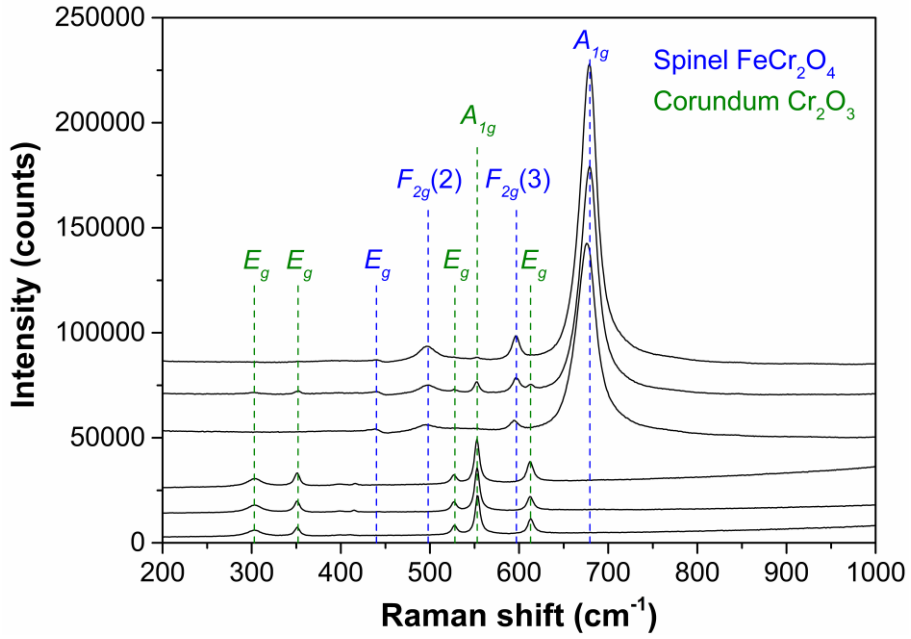

Fig. 10. Representative Raman spectra obtained by spot analyses in the oxide scales formed on P91 after 300 h exposure to molten NaCl-KCl at 700°C in flowing Ar.

Table 3
Summary of the Raman measurements and corresponding identification of the oxide compounds.

This work			References	
Structure	**Vibrational mode**	**Raman shift (cm^{-1})**	**Cr_2O_3 [58]**	**$FeCr_2O_4$ [59]**
Corundum	E_g	303	296	-
Corundum	E_g	352	350	-
Spinel	E_g	440	-	436
Spinel	$F_{2g}(2)$	498	-	493
Corundum	E_g	528	528	-
Corundum	A_{1g}	553	554	-
Spinel	$F_{2g}(3)$	597	-	591
Corundum	E_g	613	615	-
Spinel	A_{1g}	679	-	674

A pit region was further characterized by SEM and shows the distribution of fine Mo-rich particles and larger metallic particles within the salt matrix appearing as Na(K)Cl-K(Na)Cl crystallites in Fig. 11a and Fig. 11b. Local EDX measurements indicated that the larger metallic particles were rich in Fe, Mo and Ni but did not contain Cr. This suggests that Mo, Ni and a fraction of Fe were not dissolved in the NaCl-KCl eutectic. The local dissolution of P91 substrate observed in Fig. 11a strongly supports the fact that Cr is preferentially dissolved since the attack progresses at the prior austenite grain boundaries (PAGBs) by comparison with Fig. 1a. Since Cr was not distributed within the salt but always bonded to O according to the EPMA elemental mappings (Fig. 9a and Fig. 9b), it is evident that Cr atoms were transformed into soluble cations and/or Cr chlorides and were oxidized in a region with higher O^{2-} activity and/or higher O_2 partial pressure.

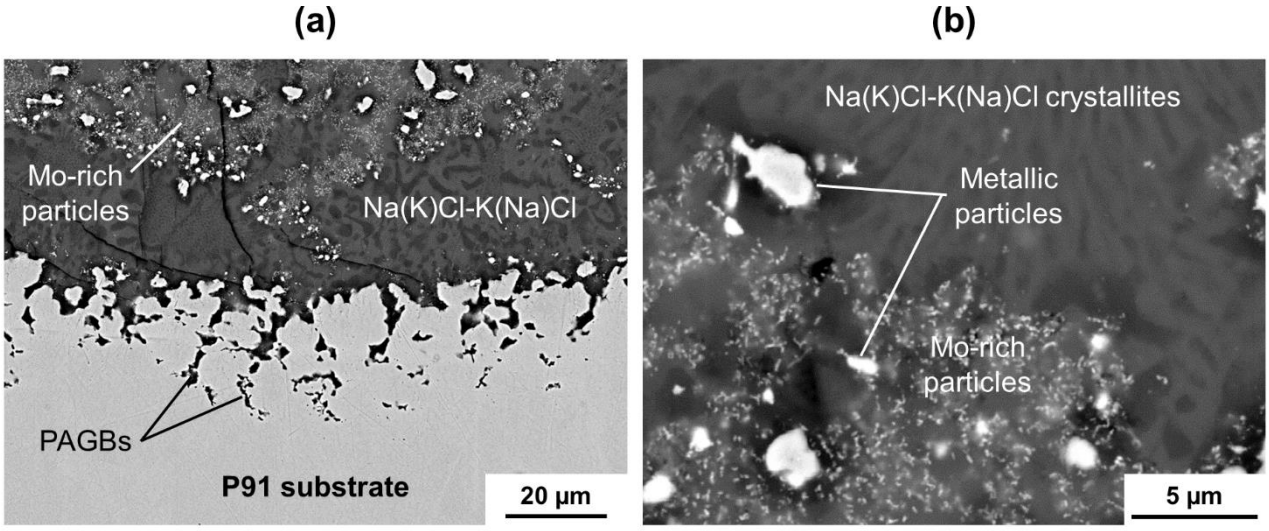

Fig. 11. BSE cross-section images of P91 after 100 h exposure to molten NaCl-KCl at 700°C in flowing Ar taken (a) at the substrate/salt interface of a pit and (b) within a pit.

3.3.2. Inconel 600 nickel-based alloy

Unlike P91, Inconel 600 was not prone to pitting corrosion in molten NaCl-KCl but exhibited very different corrosion behavior between the immersed region and the outer region as depicted on Fig. 6b. Fig. 12 presents the representative cross-section images of Inconel 600 samples after 100 and 300 h of exposure in the different locations identified in Fig. 2a. Regardless of the location, porous Cr_2O_3 scales were systematically formed. A large amount of Ni-rich metallic particles, appearing bright in BSE, are also distributed within the porous Cr_2O_3 layer (see the corresponding ellipses in Fig. 12). In addition, large Cr_2O_3 crystals are observed above the inner porous layer together with Ni-rich inclusions (Fig. 12d and Fig. 12f). Unlike P91, almost no Fe was detected in the corrosion products. The detachment of the oxide scales observed in the cross-section images of Fig. 12 most likely occurred upon cooling of the samples. In fact, a gap filled with salt is observed at the metal/salt interface in all cases, which indicates that the scales were poorly adherent to the metallic substrate. This also suggests that the oxide scales did not provide a physical barrier to the molten salt and that the electrolyte was in contact with the metallic substrate upon exposure. Note that no oxide scale was observed in Fig. 12h, which may be related to the metallographic preparation of the sample (i.e. the poorly adherent scales spalled off during the preparation).

In all locations, the corrosion attack results in the formation of a porous substrate region with a sponge-like microstructure as commonly observed for Inconel 600 exposed to molten chlorides [17,25]. It should be mentioned here that the sponge-like microstructure was systematically associated with the Cr depletion of the metallic matrix indicating that the attack progressed by selective dissolution of Cr as reported in Refs. [12,16,17,21]. As for P91, the increasing corrosion depth with time indicates that the corrosion products were not protective. Even though some intergranular attack (IGA) was observed in Fig. 12a and Fig. 12c below the corrosion front, the corrosion attack progressed independently of the grain structure of Inconel 600 (see Fig. 1b). Inconel 600 is more sensitive to corrosion in locations 3 (Fig. 12f) and 4 (Fig. 12h), i.e. in the region immersed in molten NaCl-KCl. The main difference between the top half and the immersed half of the samples after exposure lies in the formation of a porous Cr_2O_3 layer at approximately 20-30 µm depth within the substrate after 300 h exposure in locations 1 (Fig. 12b) and 2 (Fig. 12d). The presence of Cr_2O_3 was ascertained by local EDX measurements and Raman analyses.

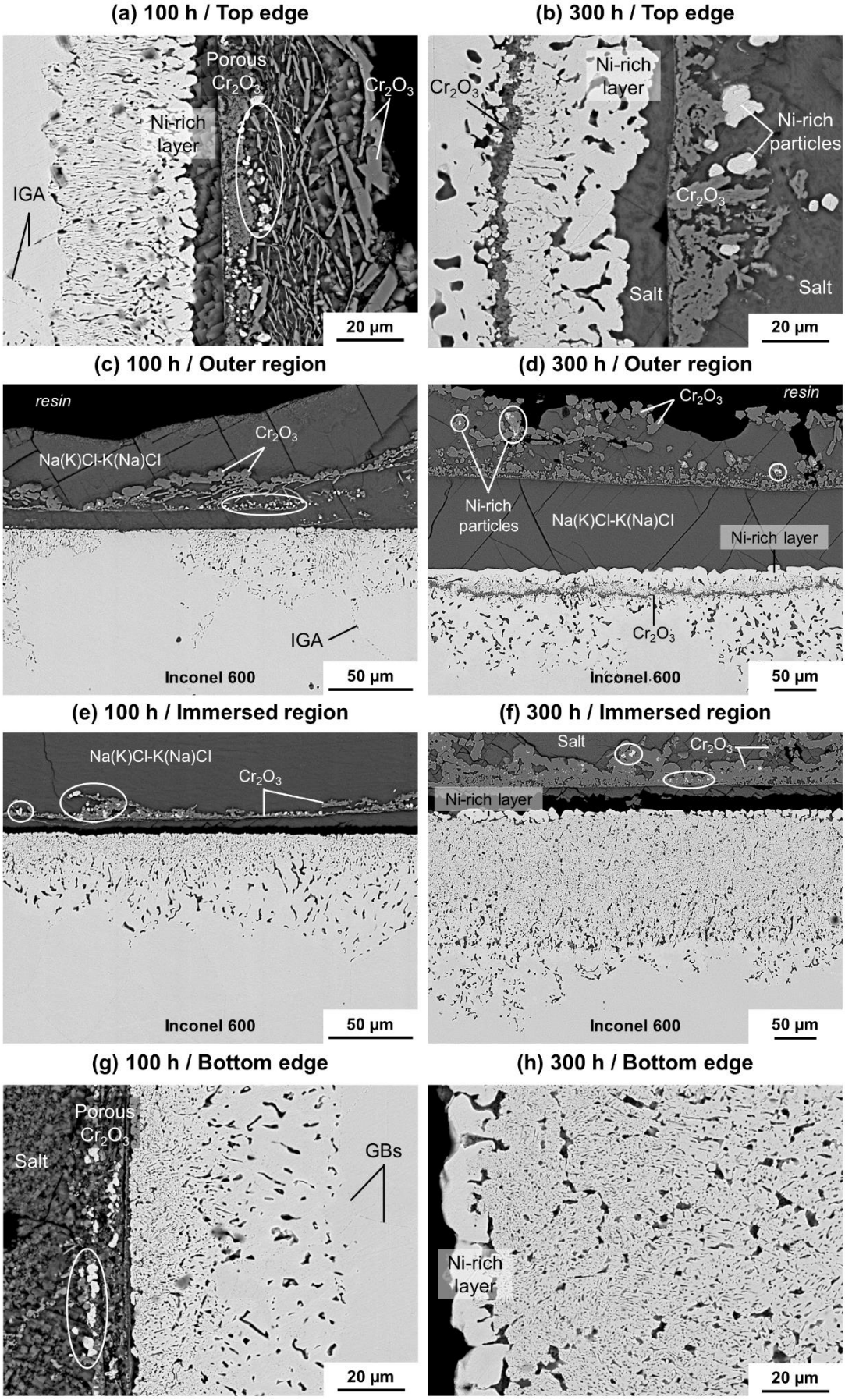

Fig. 12. BSE cross-section images of Inconel 600 samples after (a), (c), (e), (g) 100 h and (b), (d), (f), (h) 300 h exposure to molten NaCl-KCl at 700°C in flowing Ar in the different locations given in Fig. 2a. Ellipses highlight the distribution of Ni-rich particles within the scales and the salt mixture.

To further investigate the corrosion behavior of Inconel 600 in molten NaCl-KCl, EPMA elemental mappings were performed in two different regions of a sample exposed for 100 h at 700°C. Fig. 13a corresponds to the immersed region (location 3 in Fig. 2a) and Fig. 13b corresponds to a region with a lower extent of corrosion (randomly observed in location 1 in Fig. 2a). In both regions, Cr elemental mappings confirm the preferential formation of porous Cr_2O_3 scales on the surface together with the depletion of Cr in the porous substrate regions. As observed earlier, Ni and Fe-rich metallic particles, appearing bright in BSE, can be observed within the porous Cr_2O_3 scales (Fig. 13a). Such metallic particles probably resulted from their decohesion from the substrate leaving large voids in the subsurface of the substrate. In addition, the subsurface of Inconel 600 became richer in Ni with time since Cr and Mn appear to be preferentially dissolved (Fig. 13a and Fig. 13b). This Ni-rich layer is systematically observed at the subsurface of Inconel 600, even after 300 h of exposure (Fig. 12b, d, f and h), which indicates that Ni is quite resistant to corrosion in these conditions. The elemental mappings of Cl, Na and K indicate that the pores that formed within the substrate are filled with salt and, therefore, that the electrolyte was penetrating the porous microstructure of Inconel 600 most likely through capillary effects.

Since the corrosion attack was localized at the extreme surface in Fig. 13b, a cross-section image at higher magnification is given in the inset. One can see the formation of a relatively dense and continuous Cr_2O_3 scale that remained attached to the surface (confirmed by Raman analyses) whereas a porous Cr_2O_3 scale is also observed within the salt. It indicates that local breakdown of the dense Cr_2O_3 scale resulted in the internal corrosion of the substrate (Fig. 13b).

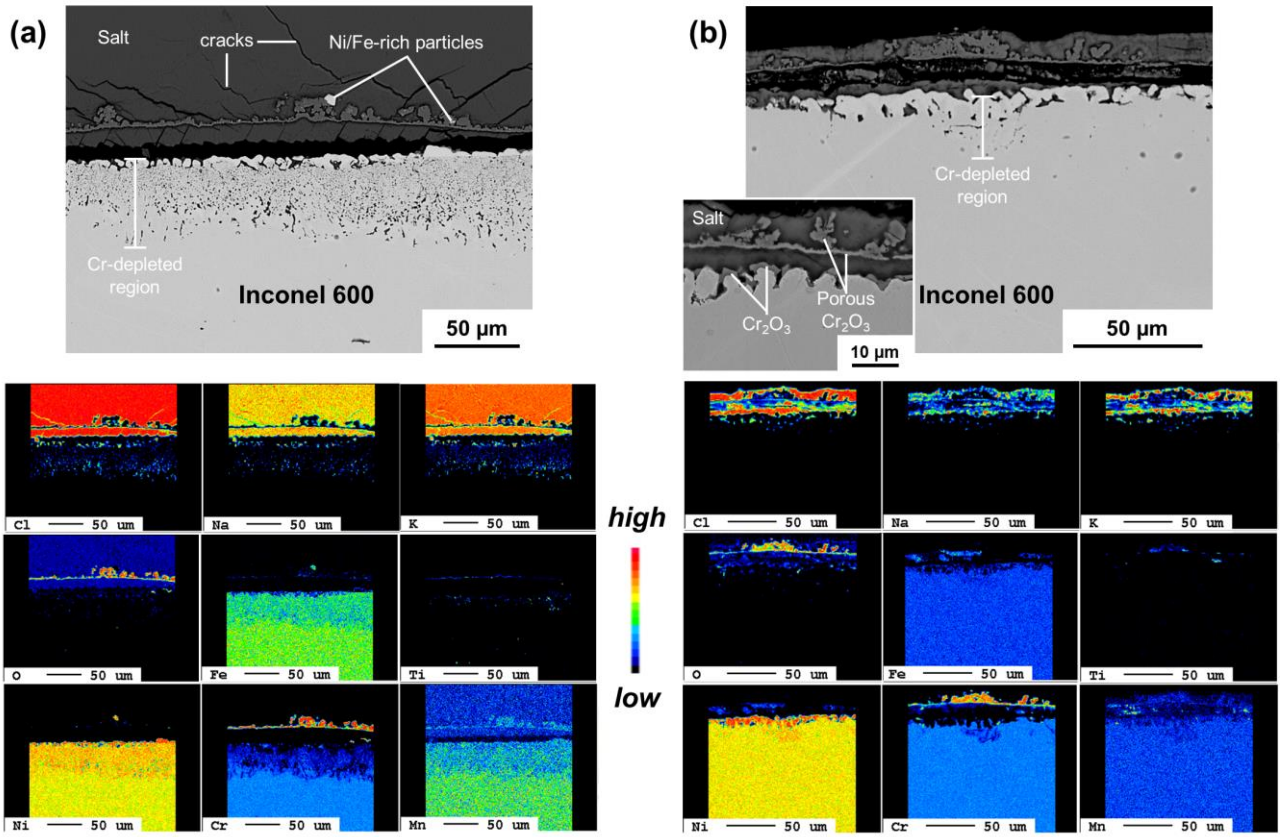

Fig. 13. BSE cross-section images and corresponding EPMA elemental mappings of Inconel 600 after 100 h exposure to molten NaCl-KCl at 700°C in flowing Ar in the (a) immersed region and (b) outer region. The inset shows a region with a low extent of corrosion and the formation of Cr_2O_3 at the metal/salt interface.

The comparison of as-received (Fig. 1b) and corroded samples (Fig. 12) of Inconel 600 indicates that the subsurface microstructure of Inconel 600 was transformed upon exposure. Therefore, further investigations were carried out at higher magnification below the Cr-depleted region showing extensive void formation (Fig. 14). The chemical contrast given with the BSE mode of the SEM highlights the distribution of fine particles within the γ-(Ni) matrix (see the highlighted areas in Fig. 14). Despite the relatively large spot resolution of the EDX technique, these particles were unambiguously enriched in chromium and in carbon in comparison to the γ-(Ni) matrix. It should be mentioned here that annealing in the temperature range of 600 to 800°C is commonly known to foster the intragranular precipitation of Cr-rich carbides in Inconel 600 of various carbon content [60-62]. The stoichiometry of such fine Cr-rich carbides, i.e. $M_{23}C_6$ and M_7C_3, is usually determined with transmission electron microscope studies [62,63]. Interestingly, the smaller voids observed in the Cr-depleted region in Fig. 14 present a diameter in the same range of order that of the Cr-rich carbide particles. This might indicate the preferential dissolution of Cr-rich phases upon exposure to molten NaCl-KCl whilst the γ-(Ni) matrix acts as the cathode as reported previously by several groups for nickel-based alloys exposed to molten chlorides [21,31,32]. In addition, a large Ti-carbide, which formed during processing of the alloy, was observed in the microstructure (Fig. 14). Such Ti-carbides do not seem to be affected by the molten salt exposure although its decohesion from the metallic matrix is observed.

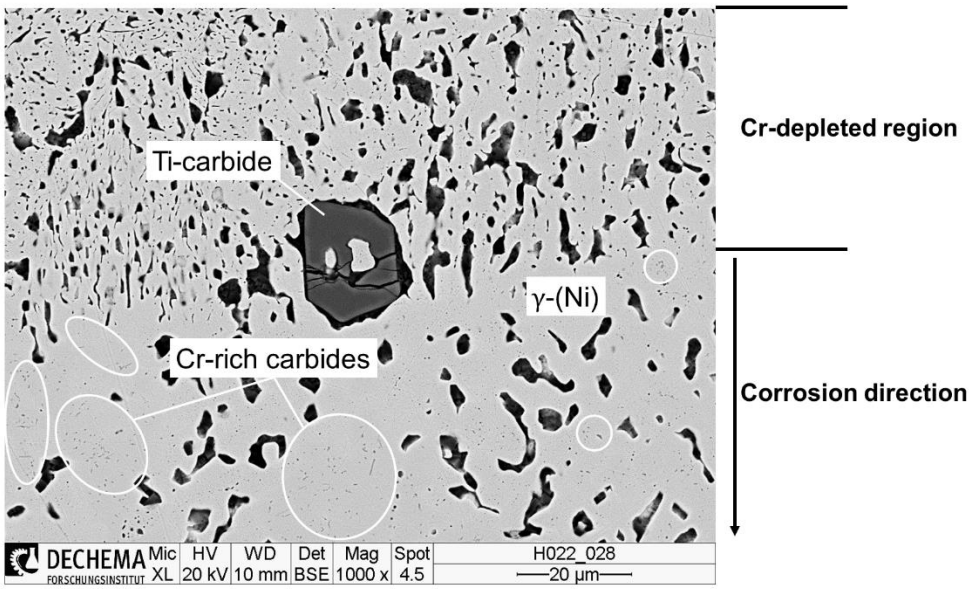

Fig. 14. BSE cross-section image showing the precipitation of Cr-rich carbides in the γ-(Ni) matrix below the Cr-depleted region for Inconel 600 after 300 h exposure to molten NaCl-KCl at 700°C in flowing Ar. The Ti-carbide formed during alloy processing is stable in the conditions of exposure.

4. Discussion

4.1. Influence of testing conditions on the corrosion kinetics

The design of the experiments presented in Fig. 2a allowed to characterize different locations for each sample corresponding to different testing conditions. On the top half of the samples (locations 1 and 2), the surfaces were initially exposed to the gas phase (Ar + 5 ppm water vapour + 2 ppm O_2) whereas the immersed half (locations 3 and 4) was embedded in the NaCl-KCl salt mixture. This leads to different O_2 partial pressure and electrochemical conditions (i.e. contact with the electrolyte) at the beginning of the exposure. Nevertheless, the salt mixture was systematically observed on the top half of the samples after exposure (Fig. 8 and Fig. 12) when the salt progressively wetted the entire surface of the samples. This implies an evolution of the boundary conditions for the top half of the samples over time whereas the initial boundary conditions are maintained for the immersed half. This evolution of the boundary conditions over time is expected to play a significant role for thermal energy storage applications with alternative filling and emptying of molten salts from the storage tanks [1,2]. Due to the electrochemical nature of the involved corrosion processes and the influence of mass transport of oxidizing species such an evolution could impact the corrosion mechanisms and local corrosion rates.

Furthermore, as mentioned by Ozeryanaya in Ref. [22], the oxidizing gases dissolved in the chloride melt such as O_2 and Cl_2 can cause corrosion of metals even if the metal surface has no direct contact with the gas phase. Owing to the limited solubility of these gases in molten alkali chlorides [22], a negative partial pressure gradient of O_2 is expected from location 1 towards location 4 upon exposure (see Fig. 2a). It can therefore be assumed that the supply of oxidants to the metal surface is the limiting step in the corrosion process. Based on this assumption, the corrosion attack of a given material should be more severe in a region with easy access of oxidizing species to the surface (i.e. thin salt layer as in locations 1 and 2 in Fig. 2a) than deep in the melt (i.e. locations 3 and 4 in Fig. 2a). This is in good agreement with the experimental corrosion rates calculated for ferritic-martensitic P91 steel in this study (see Fig. 7a and Fig. 7c). In fact, although most of the surface of P91 samples suffered from intergranular attack (IGA) localized to the prior austenite grain boundaries (PAGBs, see Fig. 8), large pits were also observed with a maximum depth of attack of 510 µm after 300 h exposure (Fig. 5a and c). The median extrapolated corrosion rate on the top side (≈ 3034 µm/year) was higher than on the immersed side (≈ 503 µm/year) whereas the propagation rates of the pits exceeded 10 mm/year. It should be noted that the initiation of pits on P91 was more likely to happen at the interfacial region between locations 2 and 3 corresponding to the salt immersion level (see Fig. 2a and the cross-section micrographs in Fig. 5c). This is related to more favorable conditions for the initiation of pits in this region as commonly reported to the "differential aeration effect" in aqueous chloride solutions [48], i.e. relatively high concentration of O_2 at the surface (cathode) and low concentration of O_2 at the pit front (anode). The larger the concentration gradient, the larger the driving force for pit growth [64].

The evolution of the iso-probability metal loss curves for P91 (Fig. 7a and Fig. 7c) indicates that the overall corrosion rates are decreasing with increasing exposure time (n values < 1). This also supports a corrosion process limited by mass transport of reactants (i.e. oxidizing species) as observed in Type-II hot corrosion conditions [53,54]. Such limitations can be explained with the growth of thick oxide scales on the surface of P91 (see Fig. 8) with relatively low electrical conductivity ($\sim 10^{-6}$ $\Omega^{-1}.m^{-1}$ for $FeCr_2O_4$ spinel [65]). The growth of oxide scales with low electrical conductivity will decrease the intensity of the cathodic reaction and, consequently, of the overall corrosion reaction (7). Unlike P91, Inconel 600 shows a linear dependence of the corrosion attack with time in the immersed region (n = 1, see Fig. 7d). This indicates that once the attack has started, the substrate is not able to reform a passive layer. The formation of porous Cr_2O_3 scales is observed together with the Cr depletion of the

substrate resulting in a porous substrate region with a sponge-like microstructure as commonly observed for nickel-based alloys exposed to molten chlorides [12,17,21,25,32]. The higher corrosion rates of Inconel 600 on the immersed side ($k_{prop,median}$ ≈ 7194 µm/year) than on the top side ($k_{prop,median}$ ≈ 1987 µm/year) and the metallographic observations of Fig. 12 clearly emphasize the susceptibility of Inconel 600 to electrochemical corrosion when exposed to molten NaCl-KCl. The higher corrosion kinetics on the immersed side than on the top side and the absence of pits also suggests that other corrosion mechanisms, or at least partially different, are involved on Inconel 600 material.

The experimental observations of the present study indicate that the oxide scales are mainly composed of $FeCr_2O_4$ spinel on P91 steel and exclusively composed of Cr_2O_3 on Inconel 600. As highlighted in the higher magnification picture (Fig. 9b), Cr_2O_3 was also locally observed on top of $FeCr_2O_4$ spinel for P91 steel. Nevertheless, it is worth mentioning that the volume fraction of $FeCr_2O_4$ is considerably larger than the volume fraction of Cr_2O_3 on most of the P91 samples' surface (see Fig. 8a-f) except in regions adjacent to a pit where a larger volume fraction of Cr_2O_3 is observed (Fig. 9a). Based on these observations, it is therefore reasonable to assume that $FeCr_2O_4$ provides a better corrosion protection than Cr_2O_3 in our experimental conditions. Despite the presence of metallic particles and of pores within the oxide scales, all playing a role in the overall electrical conductivity of the corrosion scales, it is very likely that the intrinsic electrical conductivity of the oxide compound will influence the kinetics of charge-transfer processes and its potential insulating behavior towards the underlying metallic substrate. Since Cr_2O_3 presents n-type semiconducting properties at low O_2 partial pressures [66,67], its growth probably increases the kinetics of charge-transfer processes between the melt (electrolyte) and the underlying metallic substrate in comparison with $FeCr_2O_4$ spinel. Therefore, the growth of Cr_2O_3 scales on Inconel 600 does not provide an insulating barrier effect to the electrolyte and further electrochemical attack of the substrate occurs. The distribution of Ni-rich metallic particles within the porous Cr_2O_3 scales (see Fig. 12) is also expected to increase the overall electrical conductivity of the scales. These fundamental properties could explain why the Cr_2O_3 scales formed on Inconel 600 do not provide protection in molten NaCl-KCl. Nevertheless, the exposure of the top half of the samples in the gas phase before wetting of the molten salt was associated with the formation of dense and adherent Cr_2O_3 scales on Inconel 600 (Fig. 13b). The relatively low O_2 partial pressure in the Ar atmosphere led to the formation of high-purity Cr_2O_3 scales. Any defect on the initial Cr_2O_3 scales formed on the top half of the samples would expose the metallic substrate to the molten salt thus leading to local dissolution of the substrate as observed in the inset of Fig. 13b.

4.2. Corrosion mechanisms of ferritic-martensitic P91 steel in molten NaCl-KCl

The electrochemical nature of the corrosion mechanisms implies a charge-transfer process on the metal-electrolyte interface and the mass transport of oxidants and ionic species across the diffusion boundary layer [24]. The charge-transfer rate can therefore be limited by the mass-transport rate of corrosive species presenting a maximum value for a given flowing system, which predominantly depends on the concentration gradient of the corresponding species, the flow velocity and the fluid properties [24]. As discussed in section 4.1., the corrosion rate of P91 was higher on the top side than on the immersed side of the samples suggesting the influence of the O_2 mass transport on the corrosion kinetics. The proposed corrosion mechanisms of P91 in both testing conditions are given in Fig. 15 together with the thermodynamic stability diagrams of the Fe-Cl-O and Cr-Cl-O systems at

700°C. The identification of the possible reactions and their location in the corrosion scales highlight the autocatalytic nature of the attack when O_2 is present in the system (Fig. 15).

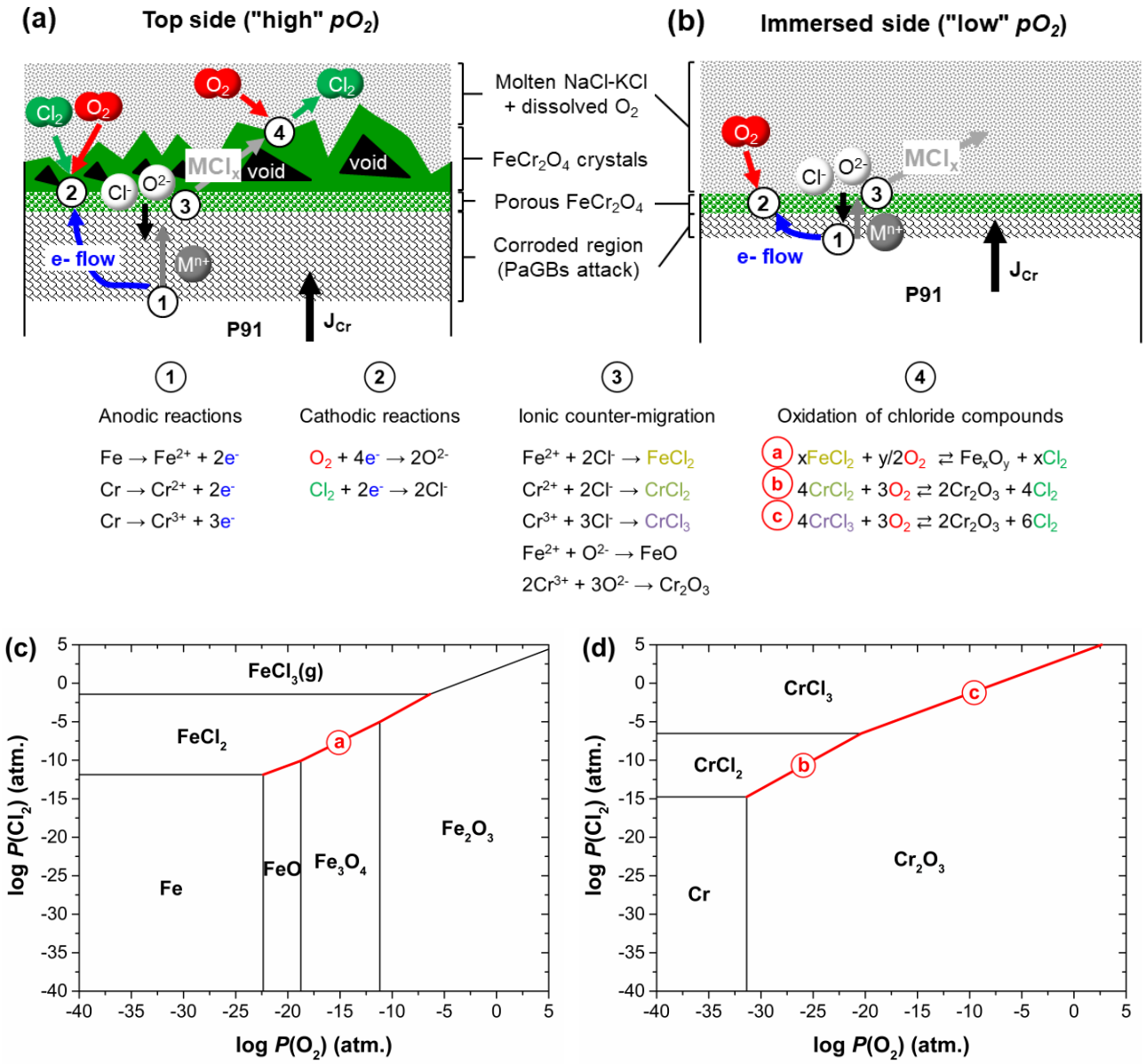

Fig. 15. (a), (b) Proposed corrosion mechanisms of P91 in molten NaCl-KCl in inert atmosphere (Ar) highlighting the influence of the residual partial pressure of O_2 on the reactions involved and (c), (d) thermodynamic stability diagrams of the Fe-Cl-O and Cr-Cl-O systems at 700°C. Lines marked with a, b and c denote the equilibrium pressures of $FeCl_2$, $CrCl_2$ and $CrCl_3$ with their respective oxides.

In the metallic substrate, the charge transfer is governed by the flow of electrons from the anode (location 1) towards the cathode (location 2). At open-circuit conditions, the intensity of the anodic reactions (i.e. metal dissolution) is indeed fed by current from the cathodic areas (i.e. reduction of O_2 and Cl_2 molecules as the stronger oxidants in the melt) [64]. Simultaneously, the anodic dissolution of metals increases the concentration of cationic species at the metal surface, which fosters the electromigration of Cl^- and O^{2-} anions to maintain charge neutrality. Depending on the local thermodynamic conditions, the counter-migration of cations and anions result in the formation of metal chlorides or oxides by ionic combination (location 3 in Fig. 15). The charge-transfer process on

the metal-electrolyte interface is therefore balanced by the mobility of ionic species in the electrolyte, as observed in molten carbonate fuel cells [68,69].

The electromigration of both Cl^- and O^{2-} at the metal surface implies a competition between chloride formation and oxide formation in location 3. Despite the very large concentration of Cl^- anions in the melt, the higher reactivity of O^{2-} anions foster the precipitation of FeO and Cr_2O_3 at the metal surface following reactions (12) and (13):

$$Fe^{2+} + O^{2-} \rightarrow FeO(s) \quad (12)$$

$$2Cr^{3+} + 3O^{2-} \rightarrow Cr_2O_3(s) \quad (13)$$

Depending on the local activity of Fe and of Cr, the simultaneous formation of FeO and Cr_2O_3 results in a porous $FeCr_2O_4$ (i.e. $FeO.Cr_2O_3$) layer. In addition to the porous $FeCr_2O_4$ layer (Fig. 15b), large $FeCr_2O_4$ crystals were also observed at the top side of the samples (Fig. 15a) after cross-section characterization of the corrosion scales formed on P91 (see Fig. 8). The formation of large $FeCr_2O_4$ crystals at the scale/melt interface suggests the occurrence of different growth mechanisms than ionic counter-migration. By analogy with the chlorine-induced corrosion of steels and Fe-based model alloys [27,28,70], such crystals are most likely formed from the reaction of volatile chloride compounds with oxygen in regions with relatively high O_2 partial pressure (location 4 in Fig. 15a). These mechanisms imply the formation of volatile chloride compounds (e.g. $FeCl_2$, $CrCl_2$ or $CrCl_3$) in location 3, their diffusion through the porous oxide scales in the outward direction and their further reaction with dissolved O_2 in location 4 forming the corresponding oxide and releasing chlorine. The released Cl_2 molecules either diffuse from the melt to the gas phase, if the Cl_2 partial pressure equilibrium between the melt and the gas phase is not reached, or diffuse back to the metal surface to adsorb and get reduced on the cathodic sites (location 2).

The stability of the chloride compounds can be predicted thermodynamically with the diagrams presented in Fig. 15c and Fig. 15d. The lines marked a, b and c correspond, respectively, to the equilibrium pressures of $FeCl_2$, $CrCl_2$ and $CrCl_3$ with their corresponding oxides. It therefore appears that a higher O_2 partial pressure is necessary to transform $FeCl_2$ than $CrCl_2$ whereas $CrCl_3$ is only expected for relatively high Cl_2 partial pressure ($> 10^{-5}$ bar). Consequently, the amount of O_2 dissolved in the melt and the mass transport of O_2 molecules will govern the reactions taking place in location 4. Increasing the O_2 supply will shift these reactions to the right, i.e. oxidation of the metal chlorides and chlorine generation. This is in good agreement with the experimental observations for P91 samples with higher corrosion kinetics and thicker oxide scales in the top side than in the immersed side (Fig. 8).

To the best of the authors' knowledge, the formation of Rinneite ($K_3NaFe^{2+}Cl_6$, i.e. $3KCl.NaCl.FeCl_2$) has yet not been reported after exposure of Fe-containing alloys to molten NaCl-KCl or other chloride mixtures. The identification of Rinneite by XRD, SEM and EDX measurements (Fig. 3 and Fig. 4a) clearly shows that a fraction of the Fe content of P91 was dissolved as Fe^{2+} cations (i.e. $FeCl_2$) within the salt mixture at 700°C. Note that Fe^{3+} species were not considered since no evidence of their formation was supported in this study. The presence of Rinneite within the salt mixture indicates that the O_2 partial pressure was too low to react with $FeCl_2$ within the melt. The higher concentration of Rinneite in the salt mixtures after 300 hours can be explained by the progressive dissolution of Fe from P91 substrate with time (especially in the pit regions). Whereas the NaCl-KCl salt mixture usually consists of fine Na(K)Cl-K(Na)Cl crystallites after cooling, the presence of Rinneite alters the microstructure of the salt mixture by forming coarse Na(K)Cl and K(Na)Cl solid solution phases in equilibrium with Rinneite (Fig. 4a and Fig. 8f). This proves that local enrichments in Fe^{2+} (i.e. $FeCl_2$) decrease the freezing temperature of the NaCl-KCl eutectic [71] and, therefore, that Rinneite is crystallizing at lower temperatures than Na(K)Cl and K(Na)Cl solid solution phases. The peritectic temperature of Rinneite is indeed 420°C [72], whereas

the miscibility gap of NaCl-KCl solid solution into Na(K)Cl and K(Na)Cl solid solutions initiates between 484°C [51] and 505°C [50].

Unlike Fe and Cr, Mo was not observed within the corrosion products and did not combine with O but remained as fine metallic particles within the melt (Fig. 11), possibly corresponding to initial Mo-rich carbides [42] or Laves phase [43]. In addition, a systematic subsurface enrichment in Mo was observed on the regions of P91 showing better corrosion resistance, as illustrated in Fig. 9b. As proposed by Sun et al. [17,21], this suggests that Mo prevents the outward diffusion of Cr along the grain boundaries and hinders the anodic dissolution of Cr and Fe (i.e. Mo atoms block the anodic sites). Such Mo enrichments in the subsurface region of P91 indicate that solid-state diffusion mechanisms also participate in the overall corrosion process [17,21]. Finally, traces of V and Mn (not shown) were found in the oxide scales formed on P91 (Fig. 9b). According to the EPMA elemental mappings, V is preferentially located in Cr_2O_3 and most likely indicates its presence as V^{3+} cations since both Cr_2O_3 and V_2O_3 have a corundum structure at high temperature and form a continuous series of solid solution [73]. In addition, when the oxygen partial pressure is lower than about $6.7x10^{-6}$ bar (i.e. 5 mTorr), which is the case in the melt, V_2O_3 was found to be preferentially grown in thin vanadium oxide films [74]. Despite the possible anodic dissolution of V into V^{3+} and of Mn into Mn^{2+}, their influence in this study seems low since both V and Mn concentrations in P91 are very small (see Table 1). Nevertheless, it suggests that alloys with high V or Mn contents may be expected to be susceptible to electrochemical corrosion in molten chlorides.

4.3. Mechanisms of pit formation on ferritic-martensitic P91 steel in molten NaCl-KCl

To support the discussion of the mechanisms of pit formation, a schematic representation is given in Fig. 16. Pitting corrosion of metals in aqueous chloride solutions is usually divided in three successive stages: passive film breakdown, metastable pitting and pit growth [64]. Pitting is autocatalytic in nature and once a pit starts to grow, the conditions developed at the metal/salt interface are such that further pit growth is promoted [64]. At open-circuit conditions, the intensity of the anodic reaction in a pit (location 1 in Fig. 16) is fed by current from the cathodic areas outside the pit (location 2 in Fig. 16) and the pit growth is therefore regulated by the reduction of O_2 and Cl_2 molecules as the stronger oxidants in the system. The pit environment is therefore progressively depleted in oxidants whereas the areas outside the pit (location 2 in Fig. 16) further shift to cathodic sites where the concentration of oxidants is higher [64]. Simultaneously, the anodic dissolution of metals following reaction (5) at the pit front (location 1 in Fig. 16) increases the concentration of cationic species, which fosters the electromigration of Cl^- anions to maintain charge neutrality. The concurrent high Cl^- concentration and low O_2 partial pressure at the pit front inhibits the passivation of the alloy and pit growth is promoted. These fundamental mechanisms are in good agreement with the microstructural observations of P91 samples exposed to molten NaCl-KCl at 700°C with no oxide formation at the pit front (see Fig. 9a), limited corrosion attack in the areas outside the pit (Fig. 8e and f) and extensive scale formation in the regions with higher O_2 partial pressure (Fig. 8c and d). This also explains the high deviation in the corrosion rates calculated for P91 steel in comparison to Inconel 600.

The high level of metal dissolution in a pit region leads to excessive formation of metal chlorides by combination of metal cations with Cl^- anions, to their outward diffusion through the porous oxide scale and, depending on the local thermodynamic conditions (see Fig. 15c and Fig. 15d), to their reaction with oxygen. Since the mass transport of O_2 molecules is the limiting step, excess metal chlorides such as $FeCl_2$ remain stable in the melt. As discussed in section 4.2., this explains the formation of Rinneite ($K_3NaFe^{2+}Cl_6$, i.e. $3KCl.NaCl.FeCl_2$) after crystallization of the salt mixture.

The EPMA elemental mappings of Fig. 9 emphasize a potential beneficial influence of Mo in preventing pitting corrosion. By analogy with the corrosion studies of ferritic steels in aqueous chloride solutions [64,75,76] and considering the prominence of solid-state diffusion mechanisms at 700°C, it can be postulated that Mo blocks the active sites for anodic dissolution and reduces the flux of cationic vacancies and the outward diffusion of Cr from the alloy thereby ennobling the areas enriched in Mo (i.e higher electrochemical potential). These hypotheses substantiate the beneficial influence of Mo in increasing the corrosion resistance of nickel-based alloys in molten chlorides [17,21].

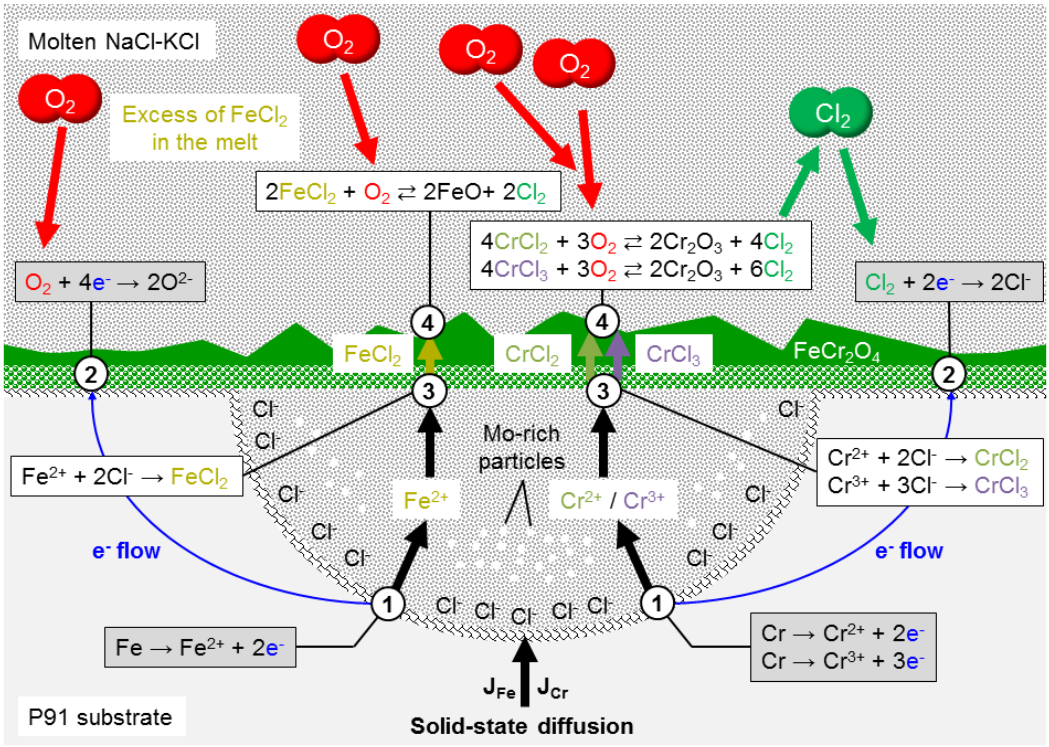

Fig. 16. Schematic representation of the autocatalytic pit growth with the main electrochemical reactions involved on ferritic-martensitic P91 steel in molten NaCl-KCl at 700°C in flowing Ar.

4.4. Corrosion mechanisms of Inconel 600 nickel-based alloy in molten NaCl-KCl

With its relatively high nickel content and low carbon solubility, Inconel 600 has long been acknowledged to be susceptible to sensitization at the grain boundaries, and the consequential intergranular corrosion leading to stress corrosion cracking in nuclear applications [60-63,77]. Nevertheless, it is also known that annealing in the temperature range of 600 to 700°C considerably increases the stress corrosion cracking resistance of Inconel 600 by forming microstructures resistant to sensitization, in which chromium carbides precipitate predominantly in the γ-(Ni) solid solution matrix instead of the grain boundaries [60-62,77]. Therefore, the initial microstructure of Inconel 600 with fine distribution of Cr-rich carbides at the grain boundaries (see Fig. 1b) is more likely to evolve upon exposure at 700°C in this study.

Considering the sponge-like microstructure of Inconel 600 after exposure to molten NaCl-KCl (see the subsurface regions in Fig. 12) and the works of Abramov and co-authors [31,32], the corrosion mechanisms of Inconel 600 are summarized in Fig. 17 with an illustration of the three different stages:

Stage 1 – Formation of excessive phases by solid-state diffusion in the alloy matrix

Since the diffusivity of C in Ni (~10^{-9} cm^2/s at 700°C [78,79]) is larger than the diffusivity of Cr in Ni (~10^{-11} cm^2/s at 700°C [80]) by approximately two orders of magnitude, the precipitation of intragranular Cr-rich carbides occurs in the γ-(Ni) solid solution matrix upon annealing at 700°C as observed in Fig. 14 and in other studies [61,63,81].

Stage 2 – Formation of micro-galvanic pairs because of dissimilar phases

The precipitation of Cr-rich phases within the γ-(Ni) solid solution matrix generates a galvanic coupling effect when in contact with the electrolyte because of a large electromotive force between the two phases [34-36]. This results in the formation of micro-galvanic pairs with Cr-rich phases acting as anodic sites and the γ-(Ni) solid solution matrix acting as the cathode [31,32].

Stage 3 – Dissolution of the least noble elements from the anodic sites of galvanic pairs

The very large cathodic area (i.e. γ-(Ni) solid solution matrix) in comparison to the small anodic areas (i.e. Cr-rich phases) results in the fast dissolution of the latter phases by anodic dissolution of Cr following the generalized reaction (5). Simultaneously, the reduction of the stronger oxidants (i.e. O_2, Cl_2) occurs on the cathode following reaction (6). As discussed in section 4.2., the charge-transfer process at the metal-electrolyte interface is balanced by ionic counter-migration of metal cations, synthesized by the anodic reactions and O^{2-} and Cl^-. Depending on the local thermodynamic conditions, the overall electrochemical reactions can therefore be written:

$$4Cr(s) + 3O_2(g) \rightarrow 4Cr^{3+} + 3O^{2-} \rightarrow Cr_2O_3(s) \quad (14)$$

$$Cr(s) + Cl_2(g) \rightarrow Cr^{2+} + 2Cl^- \rightarrow CrCl_2(l,g) \quad (15)$$

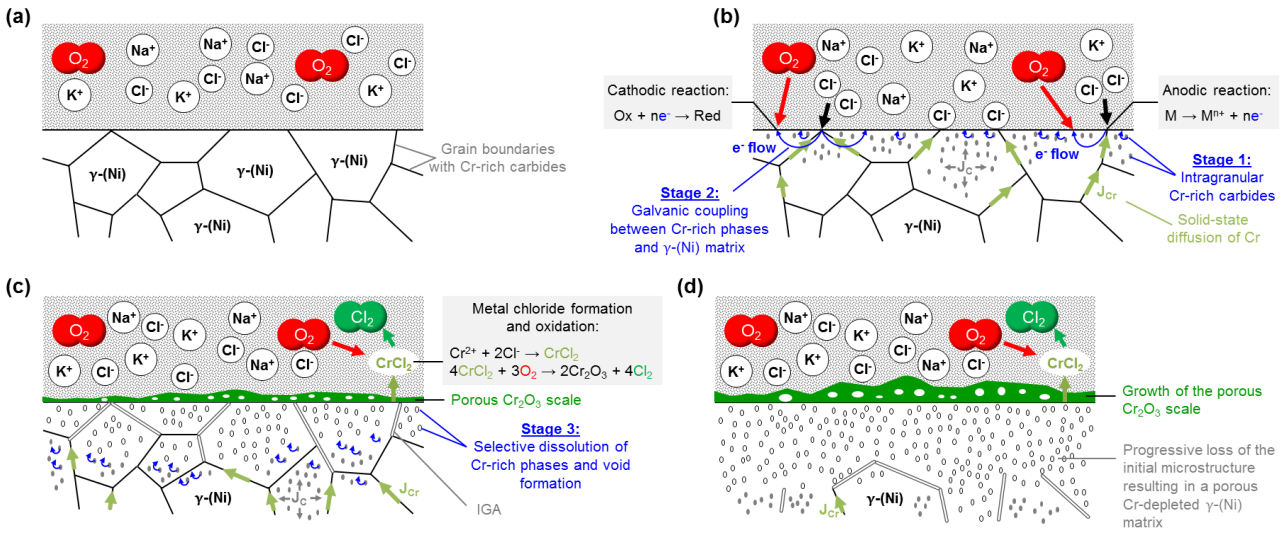

Fig. 17. Proposed corrosion mechanisms of Inconel 600 in molten NaCl-KCl in inert atmosphere (Ar) highlighting the main reactions involved and illustrating (a) the initial conditions, (b) the galvanic coupling effect between the Cr-rich phases and the γ-(Ni) matrix as well as the intragranular precipitation of Cr-rich carbides, (c) the void formation and IGA by selective dissolution of Cr and dissolution/evaporation of Cr species in the melt and (d) the resulting porous γ-(Ni) matrix depleted in Cr after longer exposure time.

Since the corrosion tests were performed at 700°C in this study, diffusion mechanisms play an important role in the overall corrosion mechanisms. Therefore, the progressive depletion of the γ-(Ni) solid solution matrix in Cr induces a positive Cr concentration gradient (noted J_{Cr} in Fig. 17) from the bulk substrate towards the surface. In

addition, it can be supposed that the C atoms set free from the dissolved Cr-rich carbides further diffuse within the substrate and form Cr-rich carbides at the corrosion front as observed in Fig. 14. The alternative precipitation and dissolution of Cr-rich carbides within the γ-(Ni) solid solution matrix hence sustains the corrosion attack of Inconel 600. It therefore appears that the systematic formation of a porous microstructure after exposure of Inconel 600 to molten NaCl-KCl is a consequence of the semi-continuous precipitation of Cr-rich carbides within the alloy matrix as first proposed by Abramov and co-workers [31,32]. These hypotheses are in good agreement with the microstructural characterization of carbide strengthened nickel-based alloys after exposure to molten chlorides [12,17,21,25,32].

Another aspect that has not yet been reported in molten chloride exposure is the distribution of Ni-rich metallic particles within the porous Cr_2O_3 scales as observed in the BSE cross-section images of Fig. 12. Such particles most likely resulted from their decohesion from the substrate by selective dissolution of semi-continuous Cr-rich phases. As aforementioned, the distribution of Ni-rich metallic particles is expected to increase the electrical conductivity of the corrosion scales, thus poisoning the ohmic drop related to the growth of oxide scales on the surface of the alloy. It should be noted here that Ni-rich metallic particles were also randomly distributed within the salt mixture after cooling (Fig. 4b), which suggests that Ni-rich phases are very stable in the melt. In addition, the random distribution of Cr_2O_3 crystals within the salt mixture (Fig. 4b) may indicate that the poorly adherent scales formed on the substrate surface spalled off during exposure and dispersed in the melt. However, such oxide crystals may also have been formed by the reaction of volatile chloride compounds (i.e. $CrCl_2$ and $CrCl_3$) with oxygen in regions with higher partial pressure of O_2.

5. Conclusions

Based on the experimental observations of this work, the following conclusions can be drawn:

(1) The water-free metallographic preparation conducted in this study was particularly helpful in preserving the corrosion scales and made possible the simultaneous characterization of the salt mixture. The additional information gained using this preparation method significantly improved the understanding of the corrosion mechanisms of ferritic-martensitic P91 steel and Inconel 600 nickel-based alloy in molten NaCl-KCl.

(2) In both P91 steel and Inconel 600, the formation of micro-galvanic pairs between Cr-rich phases (anodic sites) and the alloy matrix (cathode) led to the selective dissolution of Cr from the alloys resulting in the formation of subsurface voids. Despite the formation of pits on the surface of P91 steel with corrosion rates exceeding 10 mm/year, Inconel 600 was overall more susceptible to electrochemical corrosion. This was attributed to the greater galvanic coupling effect of secondary Cr-rich phases with the Ni-rich matrix of Inconel 600 than with the Fe-rich matrix of P91 steel. It was also proposed that the electrical conductivity of the growing corrosion scales could affect the charge-transfer processes and, therefore, the intensity of the electrochemical reactions involved.

(3) Oxygen has an active role on the corrosion mechanisms by participating on the cathodic reaction and by catalyzing the chloridation-oxidation mechanisms. Although chloridation-oxidation mechanisms participate in the overall corrosion process, the propagation of the attack within the metallic substrates is associated with electrochemical reactions.

(4) Based on the results, several technical solutions can be proposed to increase the durability of structural materials exposed to molten chlorides at elevated temperatures: reduce the carbon content of a given material

to prevent the precipitation of Cr-rich carbides within the alloy matrix, avoid alloys with dissimilar phases to prevent the formation of micro-galvanic pairs, restrict the introduction of O_2 and water in the environment, employ alloys with high Mo content to promote the passivation of the substrate by blocking the anodic sites and, finally, apply protective coatings to form insulating oxide scales upon exposure (e.g. Al_2O_3-former coatings by aluminizing).

Acknowledgements

The European Union's Horizon 2020 research and innovation program is gratefully acknowledged for funding this research (RAISELIFE, grant agreement No. 686008). The authors would like to thank Dr. Gerald Schmidt for conducting the EPMA measurements, Daniela Hasenpflug and Ellen Berghof-Hasselbächer for helping with the metallographic preparation of the samples and Susann Rudolphi for performing the optical emission spectrometry (OES) measurements.

References

[1] D.A. Baharoon, H.A. Rahman, W.Z. Wan Omar, S.O. Fadhl, Historical development of concentrating solar power technologies to generate clean electricity efficiently, *Renew. Sustain. Energy Rev. 41* (2015) 996-1027.

[2] X. Xu, K. Vignarooban, B. Xu, K. Hsu, A.M. Kannan, Prospects and problems of concentrating solar power technologies for power generation in the desert regions, *Renew. Sustain. Energy Rev. 53* (2016) 1106-1131.

[3] K. Vignarooban, X. Xu, A. Arvay, K. Hsu, A.M. Kannan, Heat transfer fluids for concentrating solar power systems - A review, *Appl. Energy 146* (2015) 383-396.

[4] A. Gastli, Y. Charabi, S. Zekri, GIS-based assessment of combined CSP electric power and seawater desalination plant for Duqum—Oman, *Renew. Sustain. Energy Rev. 14* (2010) 821-827.

[5] P. Palenzuela, G. Zaragoza, D.C. Alarcón-Padilla, J. Blanco, Evaluation of cooling technologies of concentrated solar power plants and their combination with desalination in the Mediterranean area, *Appl. Therm. Eng. 50* (2013) 1514-1521.

[6] J. Wellmann, B. Meyer-Kahlen, T. Morosuk, Exergoeconomic evaluation of a CSP plant in combination with a desalination unit, *Renew. Energy 128* (2018) 586-602.

[7] K. Vignarooban, X. Xu, K. Wang, E.E. Molina, P. Li, D. Gervasio, A.M. Kannan, Vapor pressure and corrosivity of ternary metal-chloride molten-salt based heat transfer fluids for use in concentrating solar power systems, *Appl. Energy 159* (2015) 206-213.

[8] M. Walczak, F. Pineda, A.G. Fernandez, C. Mata-Torres, R.A. Escobar, Materials corrosion for thermal energy storage systems in concentrated solar power plants, *Renew. Sustain. Energy Rev. 86* (2018) 22-44.

[9] M. Sarvghad, S. Delkasar Maher, D. Collard, M. Tassan, G. Will, T.A. Steinberg, Materials compatibility for the next generation of concentrated solar power plants, *Energy Storage Mater. 14* (2018) 179-198.

[10] A. Bonk, S. Sau, N. Uranga, M. Hernaiz, T. Bauer, Advanced heat transfer fluids for direct molten salt line-focusing CSP plants, *Prog. Energy Combust. Sci. 67* (2018) 69-87.

[11] Y. Li, X. Xu, X. Wang, P. Li, Q. Hao, B. Xiao, Survey and evaluation of equations for thermophysical properties of binary/ternary eutectic salts from NaCl, KCl, $MgCl_2$, $CaCl_2$, $ZnCl_2$ for heat transfer and thermal storage fluids in CSP, *Sol. Energy 152* (2017) 57-79.

[12] W. Ding, H. Shi, Y. Xiu, A. Bonk, A. Weisenburger, A. Jianu, T. Bauer, Hot corrosion behavior of commercial alloys in thermal energy storage material of molten $MgCl_2$/KCl/NaCl under inert atmosphere, *Sol. Energy Mater. Sol. Cells 184* (2018) 22-30.

[13] P.D. Myers Jr., D. Yogi Goswami, Thermal Energy storage using chloride salts and their eutectics, *Appl. Therm. Eng. 109* (2016) 889-900.

[14] X. Xu, G. Dehghani, J. Ning, P. Li, Basic properties of eutectic chloride salts NaCl-KCl-$ZnCl_2$ and NaCl-KCl-$MgCl_2$ as HTFs and thermal storage media measured using simultaneous DSC-TGA, *Sol. Energy 162* (2018) 431-441.

[15] G. Mohan, M. Venkataraman, J. Gomez-Vidal, J. Coventry, Thermo-economic analysis of high-temperature sensible thermal energy storage with different ternary eutectic alkali and alkaline earth metal chlorides, *Sol. Energy 176* (2018) 350-357.

[16] W. Ding, H. Shi, A. Jianu, Y. Xiu, A. Bonk, A. Weisenburger, T. Bauer, Molten chloride salts for next generation concentrated solar power plants: Mitigation strategies against corrosion of structural materials, *Sol. Energy Mater. Sol. Cells 193* (2019) 298-313.

[17] H. Sun, J. Wang, Z. Li, P. Zhang, X. Su, Corrosion behavior of 316SS and Ni-based alloys in a ternary NaCl-KCl-$MgCl_2$ molten salt, *Sol. Energy 171* (2018) 320-329.

[18] G. Mohan, M. Venkataraman, J. Gomez-Vidal, J. Coventry, Assessment of a novel ternary eutectic chloride salt for next generation high-temperature sensible heat storage, *Energy Convers. Manag. 167* (2018) 156-164.

[19] K. Vignarooban, P. Pugazhendhi, C. Tucker, D. Gervasio, A.M. Kannan, Corrosion resistance of Hastelloys in molten metal-chloride heat-transfer fluids for concentrating solar power applications, *Sol. Energy 103* (2014) 62-69.

[20] B. Liu, X. Wei, W. Wang, J. Lu, J. Ding, Corrosion behavior of Ni-based alloys in molten NaCl-$CaCl_2$-$MgCl_2$ eutectic salt for concentrating solar power, *Sol. Energy Mater. Sol. Cells 170* (2017) 77-86.

[21] H. Sun, P. Zhang, J. Wang, Effect of alloying elements on the corrosion behavior of Ni-based alloys in molten NaCl-KCl-$MgCl_2$ salt at different temperatures, *Corr. Sci. 143* (2018) 187-199.

[22] I.N. Ozeryanaya, Corrosion of metals by molten salts in heat-treatment processes, UDC 620.193.423, Plenum Publishing Corporation (1985) 184-188.

[23] A.M. Kruizenga, Corrosion mechanisms in chloride and carbonate salts, Sandia Report No. SAND2012-7594, Sandia National Laboratories (2012).

[24] S. Guo, J. Zhang, W. Wu, W. Zhou, Corrosion in the molten fluoride and chloride salts and materials development for nuclear applications, *Prog. Mater. Sci. 97* (2018) 448-487.

[25] G. Salinas-Solano, J. Porcayo-Calderon, J.G. Gonzalez-Rodriguez, V.M. Salinas-Bravo, J.A. Ascencio-Gutierrez, L. Martinez-Gomez, High temperature corrosion of Inconel 600 in NaCl-KCl molten salts, *Advances Mater. Sci. Eng.* (2014) Article ID 696081.

[26] H.J. Grabke, E. Reese, M. Spiegel, The effects of chlorides, hydrogen chloride, and sulfur dioxide in the oxidation of steels below deposits, *Corr. Sci. 37* (1995) 1023-1043.

[27] A. Zahs, M. Spiegel, J. Grabke, Chloridation and oxidation of iron, chromium, nickel and their alloys in chloridizing and oxidizing atmospheres at 400-700°C, *Corr. Sci. 42* (2000) 1093-1122.

[28] R. Bender, M. Schütze, The role of alloying elements in commercial alloys for corrosion resistance in oxidizing-chloridizing atmospheres. Part I: Literature evaluation and thermodynamic calculations on phase stabilities, *Mater. Corr. 54* (2003) 567-586.

[29] L. Krumm, M.C. Galetz, Impact of deposits and their morphology on the active corrosion of iron in chlorine – and sulfur-containing atmospheres in the temperature range 350-500°C, *Oxid. Met. 90* (2018) 365-381.

[30] I.B. Polovov, A.V. Abramov, O.I. Rebrin, V.A. Volkovich, E.I. Denisov, T.R. Griffiths, I. May, H. Kinoshita, Corrosion of stainless steels in NaCl-KCl based melts, *ECS Transactions 33* (2010) 321-327.

[31] A.V. Abramov, V.V. Karpov, I.B. Polovov, D.A. Vinogradov, V.A. Volkovich, O.I. Rebrin, Corrosion of nickel-chromium-molybdenum based alloy in chloride melts containing transition metal ions, *ECS Transactions 50* (2012) 357-366.

[32] A.V. Abramov, K.V. Dedov, A.F. Gibadullina, A.Y. Zhilyakov, V.V. Karpov, V.A. Volkovich, I.B. Polovov, Corrosive resistance of nickel Hastelloy G-35 superalloy in various aggressive media, *ECS Transactions 86* (2018) 155-162.

[33] I.B. Polovov, A.V. Abramov, V.V. Karpov, A.F. Gibadullina, A.Y. Zhilyakov, K.V. Dedov, S.V. Belikov, A.V. Shalk, V.A. Volkovich, O.I. Rebrin, Corrosion of nickel-based superalloys in molten chloroaluminates, *ECS Transactions 77* (2017) 753-766.

[34] S.N. Flengas, T.R. Ingraham, Electromotive force series of metals in fused salts and activities of metal chlorides in 1:1 molar KCl-NaCl solutions, *J. Electrochem. Soc. 106* (1959) 714-721.

[35] H.C. Gaur, H.L. Jindal, Standard electrode potentials in molten chlorides, *Electrochem. Acta 13* (1968) 835-842.

[36] H.C. Gaur, H.L. Jindal, Standard electrode potentials in molten chlorides-II, *Electrochem. Acta 15* (1970) 1113-1126.

[37] Y. Wang, H. Liu, C. Zeng, Galvanic corrosion of pure metals in molten fluorides, *J. Fluorine Chem. 165* (2014) 1-6.

[38] L.C. Olson, J.W. Ambrosek, K. Sridharan, M.H. Anderson, T.R. Allen, Materials corrosion in molten LiF-NaF-KF salt, *J. Fluorine Chem. 130* (2009) 67-76.

[39] L.C. Olson, R.E. Fuentes, M.J. Martinez-Rodriguez, J.W. Ambrosek, K. Sridharan, M.H. Anderson, B.L. Garcia-Diaz, J. Gray, T.R. Allen, Impact of corrosion test container material in molten fluorides, *J. Sol. Energy Eng. 137* (2015) 061007-1-8.

[40] W. Ding, J. Gomez-Vidal, A. Bonk, T. Bauer, Molten chloride salts for next generation CSP plants: Electrolytical salt purification for reducing corrosive impurity level, *Sol. Energy Mater. Sol. Cells 199* (2019) 8-15.

[41] J.E. Indacochea, J.L. Smith, K.R. Litko, E.J. Karell, A.G. Raraz, High-temperature oxidation and corrosion of structural materials in molten chlorides, *Oxid. Met. 55* (2001) 1-16.

[42] C. Pandey, A. Giri, M.M. Mahapatra, Evolution of phases in P91 steel in various heat treatment conditions and their effect on microstructure stability and mechanical properties, *Mater. Sci. Eng. A 664* (2016) 58-74.

[43] Z.F. Peng, S. Liu, C. Yang, F.Y. Chen, F.F. Peng, The effect of phase parameter variation on hardness of P91 components after service exposures at 530-550°C, *Acta Materialia 143* (2018) 141-155.

[44] J.D. Wang, D. Gan, Effects of grain boundary carbides on the mechanical properties of Inconel 600, *Mater. Chem. Phys. 70* (2001) 124-128.

[45] International Standard ISO, Corrosion of Metals and Alloys – Test Method for High Temperature Corrosion Testing of Metallic Materials by Immersing in Molten Salt or Other Liquids Under Static Conditions,17245 (2015).

[46] M. Sarvghad, G. Will, T.A. Steinberg, Corrosion of Inconel 601 in molten salts for thermal energy storage, *Sol. Energy Mater. Sol. Cells 172* (2017) 220-229.

[47] P. Dömstedt, M. Lundberg, P. Szakalos, Corrosion Studies of Low-Alloyed FeCrAl Steels in Liquid Lead at 750 °C, *Ox. Met. 91* (2019) 511-524.

[48] R. Jeffrey, R.E. Melchers, Effect of vertical length on corrosion of steel in the tidal zone, *Corrosion 65* (2009) 695-702.

[49] Ph. Refait, M. Jeannin, R. Sabot, H. Antony, S. Pineau, Corrosion and cathodic protection of carbon steel in the tidal zone: Products, mechanisms and kinetics, *Corr. Sci. 90* (2015) 375-382.

[50] M. Broström, S. Enestam, R. Backman, K. Mäkelä, Condensation in the NaCl–KCl system, *Fuel Process. Technol. 105* (2013) 142-148.

[51] D. Sergeev, D. Kobertz, M. Müller, Thermodynamics of the NaCl–KCl system, *Thermochim. Acta 606* (2015) 25-33.

[52] J.R. Nicholls, N.J. Simms, A. Encinas-Oropesa, Modelling hot corrosion in industrial gas turbines, *Mater. High Temp. 24* (2007) 149-162.

[53] J. Sumner, A. Encinas-Oropesa, N.J. Simms, J.R. Nicholls, Type II hot corrosion: Behavior of CMSX-4 and IN738LC as a function of corrosion environment, *Mater. Corr. 65* (2014) 188-196.

[54] B. Grégoire, X. Montero, M.C. Galetz, G. Bonnet, F. Pedraza, Correlations between the kinetics and the mechanisms of hot corrosion of pure nickel at 700°C, *Corr. Sci. 155* (2019) 134-145.

[55] T. König, X. Montero, M.C. Galetz, Hot corrosion type II of FeCr-based model alloys for boiler and heat exchanger applications, *Mater. Corr. 70* (2019) 1371-1384.

[56] International Standard ISO, Corrosion of Metals and Alloys – Method for Metallographic Examination of Samples After Exposure to High-temperature Corrosive Environments, 26146 (2012).

[57] K. Rahts, M. Schorr, C. Schwaln, M. Schütze, Water-free methods of preparation for the analyses of chlorides in the high temperature oxidation in chloride containing atmospheres, *Prakt. Metallogr. 36* (1999) 86-97.

[58] J. Mougin, T. Le Bihan, G. Lucazeau, High-pressure study of Cr_2O_3 obtained by high-temperature oxidation by X-ray diffraction and Raman spectroscopy, *J. Phys. Chem. Solids 62* (2001) 553-563.

[59] V. D'Ippolito, G.B. Andreozzi, D. Bersani, P. Paolo Lottici, Raman fingerprint of chromate, aluminate and ferrite spinels, *J. Raman Spectrosc. 46* (2015) 1255-1264.

[60] R.C. Scarberry, S.C. Pearman, J.R. Crum, Precipitation reactions in Inconel alloy 600 and their effect on corrosion behaviour, *Corr. 32* (1976) 401-406.

[61] M. Kowaka, H. Nagano, T. Kudo, Y. Okada, M. Yagi, O. Takaba, T. Yonezawa, K. Arioka, Effect of heat treatment on the susceptibility to stress corrosion cracking of Alloy 600, *Nucl. Technol. 55* (1981) 394-404.

[62] E.L. Hall, C.L. Briant, The microstructural response of mill-annealed and solution-annealed Inconel 600 to heat treatment, *Metall. Trans. A 16* (1985) 1225-1236.

[63] J.J. Kai, C.H. Tsai, T.A. Huang, M.N. Liu, The effects of heat treatment on the sensitization and SCC behavior of Inconel 600 alloy, *Metall. Trans. A 20* (1989) 1077-1088.

[64] G.S. Frankel, Pitting corrosion of metals, *J. Electrochem. Soc. 145* (1998) 2186-2198.

[65] Z. Lu, J. Zhu, E. Andrew Payzant, M.P. Paranthaman, Electrical conductivity of the manganese chromite spinel solid solution, *J. Am. Ceram. Soc. 88* (2005) 1050-1053.

[66] L. Latu-Romain, Y. Parsa, S. Mathieu, M. Vilasi, A. Galerie, Y. Wouters, Towards the growth of stoichiometric chromia on pure chromium by the control of temperature and oxygen partial pressure, *Corr. Sci. 126* (2017) 238-246.

[67] Y. Parsa, L. Latu-Romain, Y. Wouters, S. Mathieu, T. Perez, M. Vilasi, Effect of oxygen partial pressure on the semiconducting properties of thermally grown chromia on pure chromium, *Corr. Sci. 141* (2018) 46-52.

[68] P. Biedenkopf, M. Spiegel, H.J. Grabke, High temperature corrosion of low and high alloy steels under molten carbonate fuel cell conditions, *Mater. Corr. 48* (1997) 477-488.

[69] J.H. Wee, Carbon dioxide emission reduction using molten carbonate fuel cell systems, *Renew. Sustain. Energy Rev. 32* (2014) 178-191.

[70] H.J. Grabke, M. Spiegel, A. Zahs, Role of alloying elements and carbides in the chlorine-induced corrosion of steels and alloys, *Mater. Res. 7* (2004) 89-95.

[71] C. Robelin, P. Chartrand, A.D. Pelton, Thermodynamic evaluation and optimization of the (NaCl + KCl + $MgCl_2$ + $CaCl_2$ + $MnCl_2$ + $FeCl_2$ + $CoCl_2$ + $NiCl_2$) system, *J. Chem. Thermodynamics 36* (2004) 809-828.

[72] H. Fink, H.J. Seifert, Quaternary compounds in the system NaCl-KCl-$MgCl_2$, *Thermochim. Acta 72* (1984) 195-200.

[73] A.F. Reid, T.M. Sabine, D.A. Wheeler, Neutron diffraction and other studies of magnetic ordering in phases based on Cr_2O_3, V_2O_3 and Ti_2O_3, *J. Solid State Chem. 4* (1972) 400-409.

[74] S. Lee, T.L. Meyer, S. Park, T. Egami, H. Nyung Lee, Growth control of the oxidation state in vanadium oxide thin films, *Appl. Phys. Lett. 105* (2014) 223515.

[75] W.R. Cieslak, D.J. Duquette, An electrochemical study of the pit initiation resistance of ferritic stainless steels, *J. Electrochem. Soc. 132* (1985) 533-537.

[76] M. Urquidi, D.D. Macdonald, Solute-vacancy interaction model and the effect of minor alloying elements on the initiation of pitting corrosion, *J. Electrochem. Soc. 132* (1985) 555-558.

[77] G.P. Airey, Microstructural aspects of the thermal treatment of Inconel alloy 600, *Metallography 13* (1980) 21-41.

[78] J.J. Lander, H.E. Kern, A.L. Beach, Solubility and diffusion coefficient of carbon in nickel: reaction rates of nickel-carbon alloys with barium oxide, *J. Appl. Phys. 23* (1952) 1305-1309.

[79] B.S. Berry, Diffusion of carbon in nickel, *J. Appl. Phys. 44* (1973) 3792-3793.

[80] S.P. Murarka, M.S. Anand, R.P. Agarwala, Diffusion of chromium in nickel, *J. Appl. Phys. 35* (1964) 1339-1341.

[81] R.G. Aspden, G. Economy, F.W. Pement, I.L. Wilson, Relationship between magnetic properties, sensitization, and corrosion of Incoloy alloy 800 and Inconel alloy 600, *Met. Trans. 3* (1972) 2691-2697.